Acta Universitatis Sapientiae

Electrical and Mechanical Engineering

Volume 14, 2022

Sapientia Hungarian University of Transylvania
Scientia Publishing House

Contents

A. Belhanafi, Z. Driss, and M. S. Abid
Hydrodynamic Comparative Study on the Pumping Effects of a Square Tank Equipped with Single-Stage and Si-Stage Impellers............................1

S. B. A. Alammari, M. A. A. Zaini
Nanofluids in Zigzag Elliptical Tube Heat Exchanger: A Design Perspective 13

N. Menasri, S. Zergane, N. Aimeur, A. Saci
Experimental Investigation on the Coating of Nickel-Base Super Alloy Using Wire Flame Spraying...28

A. Zaatri, R. Kelaiaia
Control of Remote Robots by Means of Cell Phones 40

J. Ferencz, A. Kelemen, M. Imecs
Optimal Power Sharing Control of the Hybrid Energy Storage System of an Electrical Vehicle Along a Standard Driving Cycle.................................50

Acta Universitatis Sapientiae
Electrical and Mechanical Engineering, 14 (2022) 1–12

DOI: 10.2478/auseme-2022-0001

Hydrodynamic Comparative Study on the Pumping Effects of a Square Tank Equipped with Single-Stage and Bi-Stage Impellers

Abdelghani BELHANAFI[1], Zied DRISS[2] and Mohamed Salah ABID[2]

[1] Department of Mechanical Engineering, Faculty of Mechanics,
University of Sciences and Technology of Oran Mohamed Boudiaf (USTO-MB),
El Mnaouer, PO Box 1505, Bir El Djir 31000, Oran, Algeria,
e-mail: abdelghani.belhanafi@univ-usto.dz
[2]National School of Engineers of Sfax (ENIS), Laboratory of Electro-Mechanic Systems (LASEM), B.P. 1173, km 3.5 Soukra, 3038 Sfax, Tunisia,
e-mail: Zied.Driss@enis.rnu.tn, MohamedSalah.Abid@enis.rnu.tn

Manuscript received January 03, 2022; revised November 26, 2022

Abstract: A computational fluid dynamics simulation is done for comparative study from the pumping effect on the four surfaces of the stirred tank. The flow field generated by one-stage and bi-stage six-bladed Rushton turbine in the unbaffled square tank was studied. The Reynolds-averaged Navier-Stokes equation with steady-state multi-reference frame approach (MRF) is used to simulate hydrodynamic flow in the tank. The turbulent viscosity, the turbulent kinetic energy and mean velocity distributions obtained in vertical and horizontal plans are analyzed and discussed. We can deduce that the additional Rushton turbine in the upper part of the square tank improves the quality of the mixture.

Keywords: Square tank, CFD, single-stage turbine, bi-stage turbines, agitation.

1. Introduction

Mechanical agitation is a process used for mixing miscible fluids, which has a wide field of application, like in the preparations of industrial, chemical, and pharmaceutical products; the stirring techniques are parameters to be taken into account during the implementation of these mixtures.

Many researchers have focused on the design of agitated tanks and impeller geometry. Pericleous and Patel [1] modeled radial impeller with one or more stages, on the basis of the relative velocity of the fluid and the drag coefficients taken from the literature. Taca and Paunescu [2] studied the influence of the shape of the reservoir on the evolution of the power number, for a closed spherical vessel equipped with a Rushton turbine, while the fluid contained solid particles in suspension. Guillard and Trägårdh (2003) designed and tested a new model for estimating mixing times in aerated three-reactor stirring tanks, equipped with two, three and four impellers. The results showed that the developed analogy model is independent of the scale, the geometry of the tank, the number of impellers used, the distance between the impellers and the degree of homogeneity considered. Murthy and Joshi [4] tested multiple impeller designs namely disc turbine, a variety of pitched blades varying in blade angle and hydrofoil impeller. Woziwodzki et al. [5] studied the mixing efficiency of shear-thinning fluids using carboxy methyl cellulose sodium salt (Na-CMC) aqueous solutions of varying mass concentrations and three types of impellers (Rushton turbine (RT), six-flat-blade turbine (FBT), six-pitched-down-blade turbine (PBT)) which were mounted on a common shaft in combinations of three, four, and five impellers. Vakili et al. [6] studied the effect of different geometric parameters in stirred vessels equipped with two blades impeller (FBT2). They employed steady-state approach MRF and standard k-ε turbulence model in their parametric study. Ammar et al. [7] compared the effect of the tank design on the hydrodynamic structure generated with a pitched blade turbine by realizing three types of configurations: a flat-bottomed cylindrical vessel, a dished bottomed cylindrical vessel, and a spherical vessel using a CFD code. A comparative study conducted by Jie et al. [8] on the design of tanks, flat bottom, and dished bottom equipped with a Rushton turbine on the distribution of velocity in a transitional and turbulent flow. They found that the shapes of the bottom tank have a significant effect on flow patterns as well as on the velocity profiles below the impeller. In recent years, solid particles and mass transfer characteristics on power consumption using multi-impeller in gas-liquid stirred tank reactors have been extensively studied by Zhang et al. [9]. Gong et al. [10] studied the effect of different geometric parameters in stirred vessels with a flat square base equipped with four blades impeller on the concentration of the particles in a solid-liquid system. A comparative study conducted by Weipeng et al. [11] between liquid-level height and particle distribution in unbaffled square stirred-tank reactors was done. They concluded that the height-to-width ratio of the tank might affect the distribution of suspended particles in the flocculating system. Another interesting investigation was performed by Weipeng et al. [11], [12] on the mobile type effect of agitation and its position in a baffled stirred-tank reactor. The used geometry is a square flat bottom tank equipped with four baffles placed at 90° with a distance ratio between the impeller and the bottom which varies between C= 0.20H (30 mm), 0.27H (40 mm), 0.33H (50 mm), and 0.40H (60 mm). They confirmed that the tank with a spherical shape provides uniform flow in the whole vessel volume. The experimental study performed by Deyin et al. [13] in a flat bottomed transparent cylindrical plexiglass tank equipped with four pitched-blade impellers was performed to evaluate the influence of the impeller speed, impeller type, and impeller spacing on the solid-liquid mixing process. The experimental study performed by Fabiana et al. [14] in a baffled square tank reactor equipped with four pitched blade turbines was performed to evaluate the influence of the impeller clearance. From these anterior studies, it is clear that the design investigation of the external shape for the stirred tank is very useful.

The present work aims to determine the influence of the external design of the tank on the hydrodynamic structure of the flow. Moreover, we are interested in adding the second impeller with radial pumping direction on the four vertical walls of square vessels equipped with six flat blade Rushton turbines (RT6).

2. Stirred Tank Configuration

The design and dimensions of the stirred tanks with Rushton impellers of standard geometry used in this work are represented in *Fig. 1*. The square tanks were filled with water up to a height of $H = T$; diameter and the height H are equal to 0.5 m. The first configuration was equipped with a six-bladed Rushton turbine with a diameter d equal to $T/3$. The offset of the impeller from the vessel bottom C was equal to $T/3$. In the second configuration, the spacing between the turbines RT6 is defined by $h_1 = h_2 = T/3$.

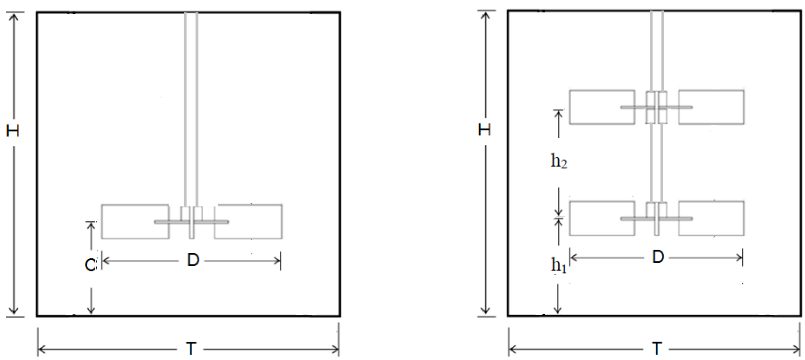

a.) One-stage turbine *b.) Bi-stage turbine*

Figure 1: Mixing vessel dimensions: *a.* Single-stage turbine. *b.* Bi-stage turbine

3. Numerical Procedure

In the turbulent regime and for an incompressible fluid, the momentum equations were solved by using the finite volume method. A pre-processor was used to discretize the 3D flow domain with a tetrahedral mesh shown in *Fig. 2*. The computational domain is reduced to 180°, with three blades and half of the shaft from the tank with one stage impeller. Periodic conditions are imposed on all properties ensuring the continuity of the computational grid in the angular direction (θ = 90° and θ = -90°).

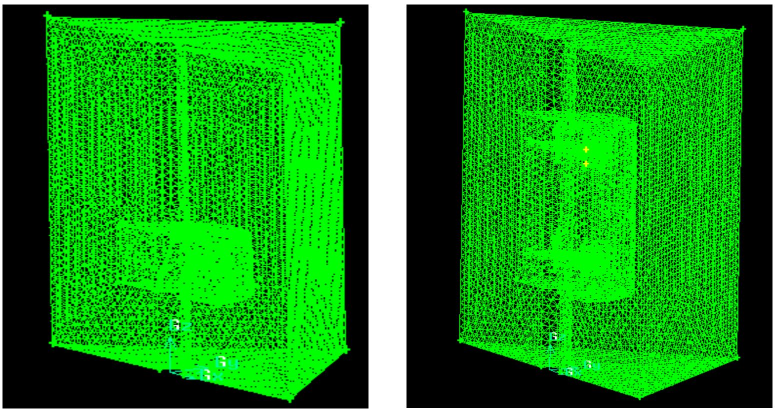

a.) Single-stage turbine *b.) Bi-stage turbine*

Figure 2: Tetrahedral mesh generation

The computational domain was divided into two blocks, the internal one containing the impellers and the external one containing the vessel walls for each case. The boundary conditions are introduced in the CFD code, using the multiple referential approaches (MRF). In this approach, the interface between the two regions is treated by the method called the frozen rotor. In this approach, the flow fields are connected at the interior surfaces (interface) separating the two domains by the method called the frozen rotor.

4. Mathematical Formulation

Governing Equations

The flow in a stirred vessel can be solved by the Navier-Stokes equations. The equations are written in their averaged form RANS (Reynolds Averaged

Navier Stokes) used in the case of a turbulent flow, due to the time of the turbulence scales.

The continuity equation is written as follows:

$$\frac{\partial \rho}{\partial t} + \nabla\left(\rho \vec{u}\right) = 0 \tag{1}$$

ρ is the density, t is the time and u is the velocity vector.

The momentum equation is written as follows:

$$\frac{\partial}{\partial t}\left(\rho \cdot \vec{u}\right) + \nabla\left(\rho \cdot \vec{u} \cdot \vec{u}\right) = -\nabla p + \nabla \tau + \vec{F} \tag{2}$$

τ is the shear stress given by:

$$\tau = -p \cdot \delta + \mu \cdot \left(\nabla \vec{u} + \left(\nabla \vec{u}\right)^T\right) \tag{3}$$

For each species, the form equation can be written as follows:

$$\frac{\partial \rho \cdot c}{\partial t} + \nabla\left(\rho \cdot \vec{u} \cdot c\right) = \nabla\left(D \cdot \nabla c - \rho \cdot \overline{c' \cdot u'}\right) + R \tag{4}$$

where c is the species concentration, D is the laminar diffusion coefficient and R represents the terms due to reactions.

For the turbulent Modeling, we have used the standard k-ε model based on the following two equations:

$$\frac{\partial \rho \cdot k}{\partial t} + \nabla\left(\rho \cdot \vec{u} \cdot k\right) = \nabla\left[\left(\mu + \frac{\mu_t}{\sigma \cdot k}\right) \cdot \nabla k\right] = P - \rho \cdot \varepsilon \tag{5}$$

$$\frac{\partial \rho \cdot \varepsilon}{\partial t} + \nabla\left(\rho \cdot \vec{u} \cdot \varepsilon\right) = \nabla\left[\left(\mu + \frac{\mu_t}{\sigma \cdot \varepsilon}\right) \cdot \nabla \varepsilon\right] = C_1 \cdot \frac{\varepsilon}{k} \cdot P - C_2 \cdot \frac{\varepsilon^2}{k} \tag{6}$$

These equations represent the conservation of the turbulent kinetic energy k and the dissipation rate of the turbulent kinetic energy ε respectively. In the above equations, the quantity P is the production of kinetic energy, which is calculated from:

$$P = \mu_{eff} \cdot \nabla \vec{u} \cdot \left(\nabla \vec{u} + \left(\nabla \vec{u}\right)^T\right) \tag{7}$$

The effective viscosity is defined as follows:

$$\mu_{eff} = \mu + \mu_t \tag{8}$$

μ_t is the turbulent viscosity, it is defined as follows:

$$\mu_t = C_\mu \cdot \rho \cdot \frac{k^2}{\varepsilon} \tag{9}$$

Equations (5) and (6) are based on exact equations and reveal required constants to model the turbulence. The "standard" constant values are:

$$C_\mu = 0.09, \quad C_1 = 1.44, \quad C_2 = 1.92, \quad \sigma_k = 1.0, \quad \sigma_\varepsilon = 1.3. \tag{10}$$

5. Numerical Results

5.1 Comparison with Experimental Results

Fig. 3 illustrates the predicted axial profile of the dimensionless radial velocity component with a Rushton turbine. With the exactly same geometrical conditions, we predicted the variation of the axial velocity along the stirred vessel. The comparison between our results and those given experimentally by Montante et al. [15] shows good agreement.

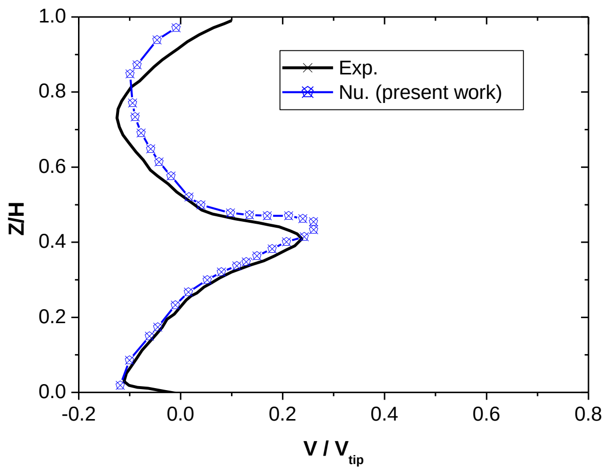

Figure 3: Axial profiles of the dimensionless radial velocity, N=240 rpm

5.2 Results and Discussion

5.2.1 Turbulent Viscosity

The horizontal presentation planes of turbulent viscosity distribution is illustrated in *Fig. 4* for both geometries at the central part of the vessel with

$z/H = 0.5$. In one stage system, the large zone of turbulent viscosity is extended throughout the volume of the tank (*Fig. 4a*). But in the second configuration, the maximum values of the turbulent viscosity are located at the shaft of the agitator (*Fig. 4b*). At the proximity of the four sidewalls of the square tanks, the turbulent viscosity drops rapidly. However, the stirring effect is still much more intense in the plane above the turbine in the first configuration (*Fig. 4a*). The turbulent viscosity is maximum in the vessel equipped with a bi-stage turbine with a 7.06 Pa·s value (*Fig. 4b*).

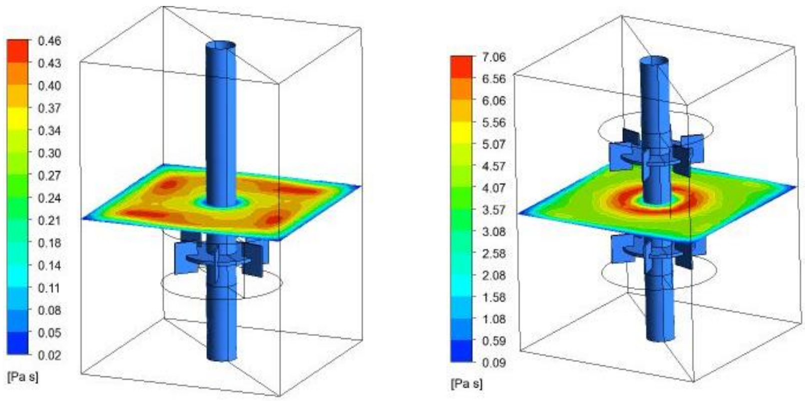

a.) Single-stage turbine *b.) Bi-stage turbine*

Figure 4: Turbulent viscosity contours in the *r*- θ plane

The turbulent viscosity generated for both cases is presented in *Fig. 5*. From these results, it is found that the position of the maximum values of turbulent viscosity is obtained at the tank with bi-stage impellers. Within one impeller system, the distribution of the turbulent viscosity is developed in the interior and superior part of the tank (*Fig. 4a*). Another remark for the second configuration (*Fig. 5b*), is that the turbulent viscosity is concentrated in space between two turbines caused a number of stages. According to these results, it is noted that the maximum value of the turbulent viscosity is obtained within two impeller stages is 6.73 Pa·s.

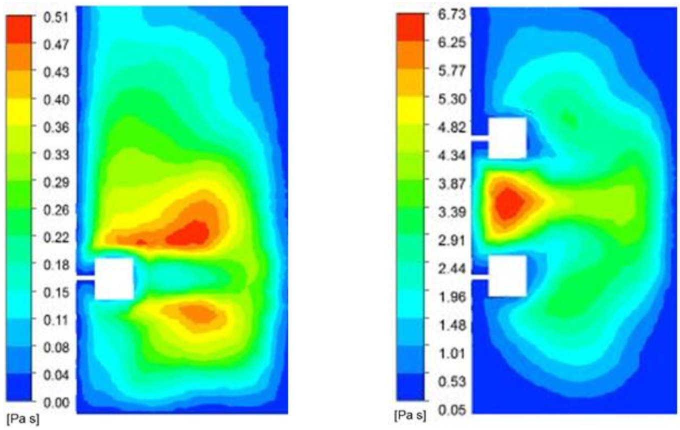

a.) Single-stage turbine *b.) Bi-stage turbine*

Figure 5: Turbulent viscosity contours in the *r-z* plane

5.2.2 Mean Velocity Distribution

5.2.2.1 Single Stage and Bi-stage Turbine in Vertical Plane

The mean velocity field produced by the Rushton turbine from the two configurations in the vertical plane is shown in *Fig. 7*. Globally, in the domain swept by the turbine blades, the velocity remains elevated enough. Within two impeller systems, the distribution of the mean velocity is developed throughout the volume of the square tank (*Fig. 6b*). Contrary to the tank with one-stage, in the upper part of the square vessel the mean velocity is very low (*Fig. 6a*). In the bi-stage vessel, the mean velocity obtained had an optimal value of 6.59 m/s. In a square tank, the use of the bi-Rushton turbines is more advantageous and increases the mean velocity.

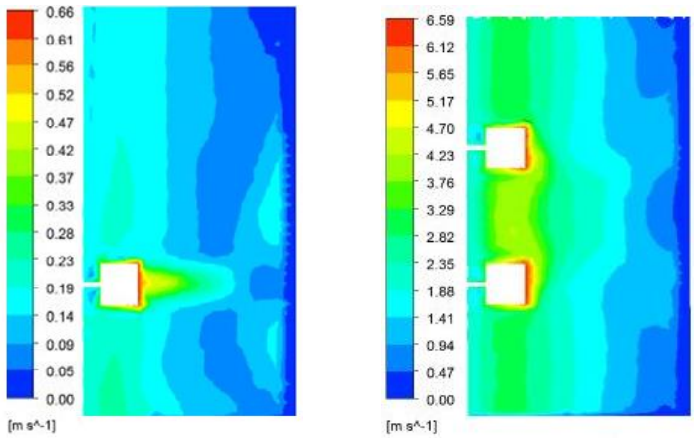

a.) Single-stage turbine *b.) Bi-stage turbine*

Figure 6: Mean velocity contours in the *r-z* plane

5.2.3 Radial Profiles

Three different axial positions were chosen for velocity and turbulent kinetic energy dimensionless for the two configurations at an angular position equal to $\theta = 0°$ following: from the half-width of the blade ($r = 0.07$ m), at the blade tip ($r = 0.085$ m) and just near the leading edge of the turbine blade ($r = 0.1$ m).

5.2.3.1 Turbulent Kinetic Energy

The profiles plotted in *Fig. 7* give the distribution of dimensionless turbulent kinetic energy for two cases at different axial positions, and are presented along the vessel radius. According to these results, it is noted that the maximum value of the kinetic energy is obtained within the bi-stage system. We can see that the region of the maximum values ($k^* > 0.075$) is located in the wake which develops at the mid-width of the blade ($r = 0.07$ m). Another point, which can be underlined, is that the increase in the number of Rushton turbines in a square tank yields higher radial pumping speed. For a location just near the region swept by the blade corresponding to ($r = 0.1$ m), the turbulent kinetic energy is dominated by maximum values in the first configuration. Outside of this area at ($r = 0.07$ m and $r = 0.085$ m), the low values of the turbulent kinetic energy are present (*Fig. 7a*). Thus, to ensure agitation in the whole square vessel volume, it is necessary to add a second turbine.

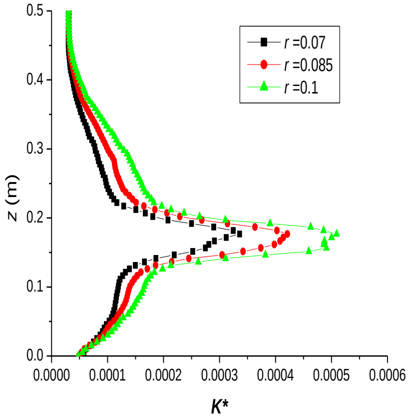

a.) Single-stage turbine

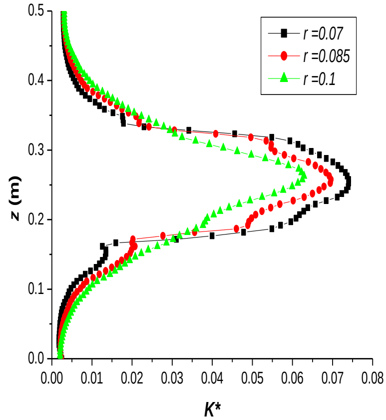

b.) Bi-stage turbine

Figure 7: Radial profiles of the turbulent kinetic energy for different blade positions (r = 0.07 m, 0.085 m, 0.1 m)

5.2.3.2 Tangential Velocity

The dimensionless tangential velocity is plotted in *Fig. 8* for the two cases studied with different axial positions, represented along the vessel radius. For the first case where just one impeller is used located at the height $z/H = 0.33$ of the vessel, the tangential circulation can't reach the free surface. At mid-width blade ($r = 0.07$ m) the optimum velocity obtained for a bi-stage tank is $W/V_{tip} = \pm 0.45$. For any case studied, the minus sign of velocity indicates the existence of a recirculation flow. The low values of dimensionless tangential velocity are obtained at ($r = 0.1$ m) in the area swept by one impeller (*Fig. 8a*). In *Fig. 8b*, we remark that the chaotic regions produced between impellers are intensified for the second case, giving better performance. If another impeller is added at the upper part of the square vessel, that can ensure mixing at this space.

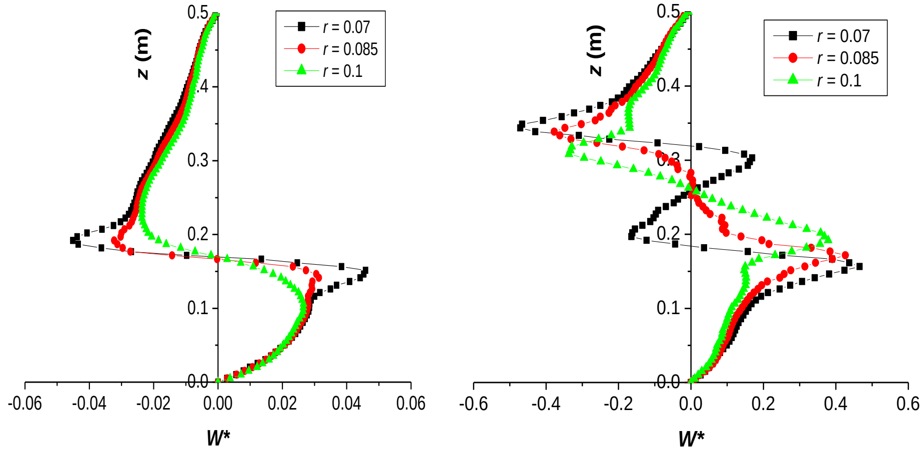

a.) Single-stage turbine *b. Bi-stage turbine*

Figure 8: Radial profiles of the tangential velocity for different positions of the blade (r = 0.07 m, 0.085 m, 0.1 m)

6. Conclusion

The aim of the investigation in this work was to determine the effect of adding the second Ruston turbine with radial pumping direction on the four vertical walls of the square vessel. From the presented results the following conclusions can be deduced:

Within one stage Rushton turbine, the shape of the wake of turbulent viscosity is more extended in the upper part of the square tank. Contrary to the square tank with bi-stage Rushton turbines, the turbulent viscosity is concentrated in the space between two impellers. For the two planes just below and above the Rushton turbine, a large zone of maximum velocity is extended to the solid walls in a square tank equipped with a single impeller. As can be deduced, for a bi-stage system the typical double loop flow circulation of tangential velocity is apparent throughout the volume of the square tank. This dynamic phenomenon is absent in the square stirred vessel with a single Rushton turbine. The increased number of impellers RT6 in a square tank plays an important role by improving the operating conditions of stirring and mixing. We can conclude that, the use of the bi-Rushton turbine at axial position z/H = 0.66 in the square tank is more advantageous than one stage turbine and increases the performance of agitation operation.

References

[1] Pericleous, K.A. and Patel, M.K., "The modelling of tangential and axial agitators in chemical reactors", *Physico. Chem. Hydrodyn.*, 8, pp. 105–123, 1987.

[2] Taca, D.C. and Paunescu, M., "Power input in closed stirred vessels", *Chemical Engineering Science.*, 56, pp. 4445–4450, 2001.

[3] Guillard, F. and Trägardh, C., "Mixing in industrial Rushton turbine agitated reactors under aerated conditions", *Chemical Engineering and Processing.*, 42, pp. 373-386. 2003.

[4] Murthy, N.B. and Joshi, J.B., Assessment of standard k-ε, RSM and LES turbulent models in a baffled stirred agitated by various impeller designs", *Chemical Engineering Science.*, 63, pp. 5468–5495, 2008.

[5] Woziwodzki, S., Broniarz, P.L. and Ochowiak, M., "Transitional mixing of shear-thinning fluids in vessels with multiple impellers", *Chemical Engineering and Technology.*, 33(7), pp. 1099–1106, 2010.

[6] Vakili, M.H., Nasir, M. and Esfaharry, B., "CFD analysis of turbulence in a baffled stirred tank, a three-compartment model". *Chem. Eng. Sci*., 64, pp. 351-362, 2009.

[7] Ammar, M., Driss, Z., Chtourou, W. and Abid, M. S., "Effect of the Tank Design on the Flow Pattern Generated with a Pitched Blade Turbine". *International Journal of Mechanics and Applications*., 2(1), pp. 12–19, 2012.

[8] Jie, D., Binjie, H., Andrzej, W. P., Xiaogang, Y. and Nicholas, J. M., "The Effect of bottom shape and baffle length on the flow field in stirred tanks in turbulent and transitional flow", *International Journal of Mechanical*., 10(9), pp. 10005417, 2016.

[9] Zhang, J., Zhengming G., Yating, C., Huayu, C., Ziqi, C. and Yuyun, Bao., "Power consumption and mass transfer in a gas-liquid-solid stirred tank reactor with various triple-impeller combinations", *Chemical Engineering Science*., 170, pp. 464–475, 2017.

[10] Gong, H., Huang, F., Li, Z., Gao, Z. and Derksen, J. J., "Mechanisms for drawdown of floating particles in a laminar stirred tank flow", *Chemical Engineering Journal.*, 346, pp. 340-350, 2018.

[11] Weipeng, H., Lianpeng, X., Beata, G., Jun, N. and Zhou, S., "Comparative analysis on flocculation performance in unbaffled square stirred tanks with different height-to-width ratios: Experimental and CFD investigations", *Chemical Engineering Research and Design.*, 132, pp. 518–535, 2018.

[12] Weipeng, H., Zhoulong, X., Ziyue, Z., Maolin, H. and Mengmeng, Pan., Effect of impeller clearance on floc growth behaviors in a baffled square stirred-tank reactor, *Separation and purification technology*., 212, pp. 233–244, 2019.

[13] Deyin, G., Chao, C., Zuohua, L. and Yundong, W., "Numerical simulation of solid-liquid mixing characteristics in a stirred tank with fractal impellers", *Advanced Powder Technology*., 30, pp. 2126–2138, 2019.
Fabiana M. B. Coelho, A. M. Botelho, O.F. Ivo, F. I. Priscilla, F. F. A, Tatiana F. F, "Volumetric mass transfer coefficient for carbon monoxide in a dual impeller stirred tank reactor considering a perfluorocarbon–water mixture as liquid phase", *Chemical Engineering Research and Design.*, 143, pp. 160–169, 2019.

[14] Montante, G and Magelli, F., "Liquid homogenization characteristics in vessels stirred with miltiple Rusthton turbines mounted at different spacings, CFD study and comparison with experimental data", *Chemical Engineering Research and Design*, 82 (A9), pp. 1179–1187, 2004.

Acta Universitatis Sapientiae
Electrical and Mechanical Engineering, 14 (2022) 13–27

DOI: 10.2478/auseme-2022-0002

Nanofluids in Zigzag Elliptical Tube Heat Exchanger: A Design Perspective

Sumaia Bugumaa Abubaker ALAMMARI[1],
Muhammad Abbas Ahmad ZAINI[2]

[1] Department of Chemical Engineering, Faculty of Chemical & Energy Engineering, Universiti Teknologi Malaysia, 81310 UTM Johor Bahru, Johor, Malaysia,
e-mail: sumaia.alammari@su.edu.ly
[2] Centre of Lipids Engineering & Applied Research (CLEAR), Ibnu-Sina Institute for Scientific & Industrial Research, Universiti Teknologi Malaysia, 81310 UTM Johor Bahru, Johor, Malaysia, e-mail: abbas@cheme.utm.my (corresponding author)

Manuscript received October 05, 2022; revised November 26, 2022

Abstract: Nanofluids contain nanometer-sized particles in suspension to enhance heat transfer by increasing the thermal conductivity. This paper provides an overview of particle size and volume fraction of nanofluids, and their roles in enhancing the heat transfer. Often, the transfer of heat is enhanced by dispersed particles with small diameter and high concentration despite some debate about the governing effects. The design of elliptical cross-section and zigzag tube also sheds insight into augmenting heat transfer for future research directions and applications.

Keywords: Elliptical cross-section, heat transfer coefficient, nanofluid, nanoparticle, zigzag tube.

1. Introduction

Heat is essentially migrated by temperature gradient, from hot to cold region. This principle has been applied in various chemical and industrial processes to exchange heat between two working fluids [1]. Heat transfer enhancement can be categorized as passive and active techniques. Active techniques depend on external source of power to induce the heat transfer process, whereas passive techniques rely on equipment design. Both techniques are aimed to reduce energy requirement to yield more efficient heat transfer process [2].

Water, gasoline, and ethylene glycol are some of the commonly used working fluids in heat exchangers, but their thermal conductivities are low. Consequently, the heat transfer is inefficient. To overcome this drawback, suspended nano-sized particles can be introduced in the base fluids to improve the thermal conductivity [3]. A suspension of CuO in ethylene glycol elevates the thermal conductivity by 20% [4]. Similarly, the conductivity is intensified when CuO nanoparticles are dispersed in water [5]. Recently, the addition of ZrO_2, TiO_2, and Al_2O_3 nanomaterials as compared to plain water gives rise to the outlet temperature of cold nanofluids by 7.7%, 11.3% and 17.4%, respectively due to the elevation of heat capacities [6]. Zinc oxide, silicon oxide, and other metal oxides are promising sources of nanoparticles to form nanofluids with varying results to improve the heat transfer in heat exchangers [7].

The fluid flow is generally categorized as laminar and turbulent. The flow regime is important in the design and operation of any fluid system. Several studies used the flow regimes to improve the heat transfer of nanofluids [8], [9]. A significant heat transfer performance at laminar regime is demonstrated by Al_2O_3 nanofluid in a copper tube [10]. Conversely, Kumar [11] reported the improvement of heat transfer by Al_2O_3 nanofluid at low volume fraction under turbulent flow inside a pipe of constant wall temperature. In a related work, Danook et al. [12] evaluated the heat transfer of nanofluid at Reynolds number between 1×10^4 and 1×10^5, as a specific transition from laminar to turbulent flow regime.

The volume fraction of particles (volumetric concentration) can also affect the thermal conductivity of a nanofluid. The manipulation of volumetric concentration is imperative to bring a positive response towards heat transfer performance at constant temperature for a fixed diameter of nanoparticles [13]. Fule et al. [14] used a 0.1 vol.% of CuO that brings a better heat transfer coefficient by 37.3% as compared to the base fluid, whereas the magnitude is even higher by 77.7% at 0.5 vol.%. The increase of flow rate of CuO nanofluid exhibits a significant increase in heat transfer coefficient, suggesting that the amount of CuO in the base fluid enhances the heat transfer coefficient. The influencing factors of particle diameter and volume fraction in heat transfer are noticeable. For instance, the decrease of particle size and the increase of volume fraction improve the heat transfer coefficient of the Al_2O_3 nanofluid in a helical coil at constant temperature [15].

The design of heat exchanger is generally composed of smooth circular tube. The thermal and hydrodynamic properties in circular tube have been investigated for many years, owing to its significance and relevance in industrial processes, in spite of low efficiency [16]. The poor heat exchanger efficiency can be partly resolved through design by means of internal fins [17], external fins [18], corrugated tube [19], square pipe [20] and hexagonal duct [21]. Theoretical studies about the elliptical ducts showed that flattening the duct by maintaining the constant cross-sectional area increases considerably the heat transfer coefficient [22], [23].

The old design of heat exchanger is normally confined to straight tube configuration. Now, it begins to evolve, aimed at improving the heat transfer coefficient. Parlak [24] studied heat transfer coefficient of water in three types of microchannels, i.e., straight, wavy, and zigzag, for which Ansys calculations have been used to optimize the geometry. The zigzag tube is the optimum geometry with high heat transfer coefficient compared to straight channel. Recently, Kishan et al. [2] also reported an improvement in heat transfer by zigzag tube, outweighs that of straight tube and U-shaped tube.

2. Nanofluid

A nanofluid is a mixture of nanoparticles (metal oxides) and base fluid (e.g., water and ethylene glycol). Often, the nanofluid is more viscous than base fluid. Nonetheless, the pumping power needs for the viscous fluid are compensated by the increase of thermal conductivity and heat transfer coefficient [25-27]. Generally, metal oxides increase the intensity of the heat transfer in nanofluids [28]. The thermal transfer of aluminum oxide nanofluids increases by 20% to 41% depending on base fluids [29]. Copper oxide, zinc oxide, silicon oxide and titanium oxide are examples of metal oxides that demonstrate similar influence on the thermal conductivity. For any volume fractions, zinc/water nanofluid displays an improved heat transfer compared to the base fluid. As compared to the base fluid, a 46% increase of heat transfer was recorded [30]. Similarly, a small fraction of SiO_2/water nanofluid elevates the heat transfer coefficient by 50% [31]. Table 1 summarizes the heat transfer improvement using zinc oxide and silicone oxide nanofluids.

Table 1: Heat transfer improvement using zinc oxide and silicone oxide nanofluids

Nanofluid	Finding	Reference
Al_2O_3/water, ZnO/water	Al_2O_3 performs better than ZnO as nanofluid for heat transfer.	Rasheed et al. [32]
ZnO@TiO_2/water	Maximum improvement at 0.1 wt.% concentration, 47% higher than water alone. ZnO and TiO_2 mixture elevates the overall heat transfer coefficient.	Ahmed et al. [33]
ZnO/water	The heat transfer coefficient is higher at 0.44 vol.%.	Safir et al. [34]
TiO_2@ZnO/water	Heat transfer rate increases at 2.0 vol.% of TiO_2 and 1.5 vol.% of TiO_2@ZnO hybrid.	Lahari et al. [35]
Al_2O_3/water, SiO_2/water, ZnO/water	Higher overall heat transfer coefficient by ZnO > Al_2O_3 > SiO_2.	Shahrul et al. [36]
ZnO/water	Heat transfer is enhanced by 46% compared to water alone at 0.2 vol.%.	Ali et al. [37]

Nanofluid	Finding	Reference
Al_2O_3/water, CuO/water, SiO_2/water	SiO_2/water exhibits only a slight increase of thermal performance by 2.5% at 4 vol.% compared to water.	Noorbakhsh et al. [38]
SiO_2/water	Low concentration of SiO_2 increases the heat transfer rate by 50% compared to water.	Hussein et al. [31]
TiO_2/water, SiO_2 /water	SiO_2 nanofluid increases the heat transfer rate by 18% compared to water.	Hussein et al. [31]
CuO, Al_2O_3, SiO_2 in water and ethylene glycol	Small particle diameter increases the viscosity. Nusselt number increased by 35% for 6 vol.% CuO.	Namburu et al. [39]

2.1 Particle Size of the Nanofluid

The size of nanoparticles can affect the thermal conductivity and viscosity of the nanofluid. There is a long debate about the relationship between nanoparticle size and viscosity. For instance, Namburu et al. [39] reported that nanoparticles with small diameter render high viscosity of nanofluid and high Nusselt number, and the heat transfer coefficients of Al_2O_3 and SiO_2 are better than that of CuO. Rudyak et al. [40] used Brookfield viscometer to quantify the effect of particle diameter (10 to 150 nm) in SiO_2/water, Al_2O_3/water, and TiO_2/water nanofluids at fixed volume fraction of 2%. It was found that the viscosity decreases with increasing particle diameter. Also, Nguyen et al. [41] showed that the viscosity of some nanofluids remain unchanged for concentrations less than 4 vol.%. However, as the volume concentration exceeds this limit, the particle size seems to have considerable effect on fluid viscosity. On the contrary, Lu and Fan [42] reported an increase in viscosity of the aluminum oxide/ethylene glycol nanofluid as the particle size decreases. Similarly, copper oxide, aluminum oxide and silicon oxide show the same pattern of increasing viscosity for smaller particle size in water as base fluid [43].

The particle diameter plays a considerable role in improving the conductivity of the nanofluid. Eastman et al. [44] showed that the thermal conductivity is more responsive to the particle size than to the volume fraction. Chon et al. [45] reported a decreasing trend of conductivity of Al_2O_3/water nanofluid with increasing particle diameter from 11 to 150 nm. This is due to Brownian motion that has a great influence on heat transfer; the smaller the particle, the faster the Brownian movement, thus the higher the conductivity that is responsible for the increase in heat transfer. Karthikeyan et al. [46] recognized the increase of thermal conductivity of copper oxide at 1 vol.% due to its smaller particle size of 8 nm. On the other hand, Beck et al. [47] showed the opposite perspective, whereby the conductivity decreases with decreasing particle size of less than 50 nm due to the increase in dispersion of smaller particle phonon (photon scattering at the solid-liquid interface). The thermal conductivity of aluminum oxide nanofluid was measured for different particle diameters of 8 to 282 nm using hot wire technique. The thermal conductivities of nanofluids made up of SiO_2/water, Al_2O_3/water, and TiO_2/water for particle size ranging from 10 to 150 nm reveal that as the size increased, the thermal conductivity also increased [40].

2.2 Volume Concentration of the Nanofluid

Volume concentration of the metal oxide in nanofluid can also affect the thermal conductivity and viscosity. Usually, the higher the volume concentration, the greater the conductivity. The conductivity of nanodiamond/water was studied as a function of concentration by KD_2-Pro equipment using transient line heat source method [48]. The thermal conductivity increased nonlinearly as the concentration increased from 0.8 to 3%. Similarly, Sundar et al. [49] reported the same pattern of increasing thermal conductivity with concentration of Fe_3O_4/water nanofluid that is ranging from 0.2 to 2%. As the concentration of metal oxide increases, the Brownian motion of the nanoparticles induces micro convection surrounding the liquid molecules, so elevating the conductivity. The thermal conductivities of Al_2O_3, CuO and TiO_2 nanofluids also improved as the volume fraction increased because of particle collision and Brownian motion [50], [51].

There is also a direct correlation between concentration and viscosity, whereby the higher the concentration of nanoparticles, the higher the viscosity. The increase in concentration of Al_2O_3/water and CuO/water nanofluids results in the increase of viscosity. For example, at particle diameter of 47 nm, the viscosity of Al_2O_3 nanofluid surges from 1.12 to 1.6 cP, and 3 to 5.2 cP at volume fractions of 1 to 4%, and 9 to 12%, respectively [41].

3. Elliptical Cross-Section Tube Heat Exchanger

The use of elliptical tubes has been an excellent approach to improve the hydraulic and thermal performance of the heat exchanger. Alias et al. [52] studied the thermal performance of Al_2O_3/water and ZnO/water nanofluids in a helical microtube coil with circular, oval, and elliptical tube cross-sections, wherein Al_2O_3 exhibits a better heat transfer than ZnO by circular cross-section. In a related work, the heat transfer was numerically explored for SiO_2 and ZnO nanofluids in elliptical cross-section of helical copper tube as shown in *Fig. 1*. For turbulent flow of Reynolds number 4×10^3 to 2×10^4, the Nusselt number rises as the volume fraction increases. At pitch diameter of 18 mm, ZnO at volume fraction of 2% exhibits a higher heat transfer coefficient.

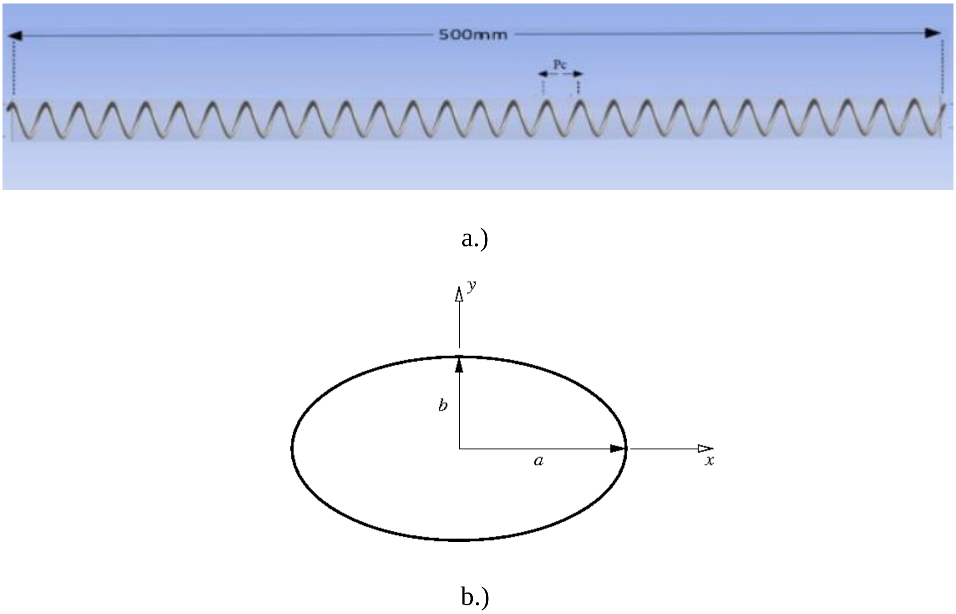

Figure 1: Helical tube (a) with elliptical cross-section (b) [52]

Ahmadi et al. [53] numerically evaluated the heat transfer for CuO at volume fractions of 1 to 4% in circular pipe fitted with elliptical-cut and square-cut twisted tapes, in which the elliptical-cut with 4 vol.% CuO depicts an increase in thermal performance by 21% compared to the water alone, and 26% compared to square-cut with the same fraction of nanofluid. Qi et al. [54] studied the effect of TiO_2/water in elliptical tubes with a built-in turbulator that shows a 33.8% improvement in heat transfer using 0.5 wt.% nanofluid. An increase of 44.3% in heat transfer rate was recorded using 0.2 vol.% of Al_2O_3/water in elliptical cross-section tube [55]. Likewise, Al_2O_3/methanol nanofluid demonstrates a substantial increase of 50 to 70% in the overall heat transfer coefficient via numerical simulation of laminar flow in an elliptical duct [56]. Another form of the tube design is elliptical tube inside a circular tube. The elliptical annulus tube may improve the friction factor and heat transmission by 6 and 19%, respectively when compared to circular annulus [12], [57]. The Nusselt number and friction factor often increased with decreasing particle diameter but increased with volume concentration. Table 2 summarizes the findings of elliptical cross-section tube heat exchangers.

Table 2: Elliptical cross-section tube heat exchangers

Cross-section	Finding	Reference
Helical microtube coil (circle, oval, elliptical)	Al_2O_3 is better than ZnO. Best performance at volume concentration of 2%.	Rasheed et al. [32]
Copper elliptical tube, helical micro pipe	ZnO at 2 vol.% endows a high Nusselt number at pitch diameter of 18 mm.	Alias et al. [52]
Circular pipe fitted with elliptical-cut twisted tape	A 6.6% improvement compared to square-cut twisted tape.	Ahmadi et al. [53]
Elliptical tubes with a built-in turbulator	Thermal performance increased by 33.8% compared to water.	Qi et al. [54]
Elliptical-shaped cross-section	Heat transfer rate increased by 44.3% compared to water.	Chaurasia et al. [55]
Elliptical duct	Heat transfer coefficient improved by 25%. Overall heat transfer coefficient increased by 50 to 70%.	Ragueb et al. [56]
Elliptical tube inside a circular tube	Elliptical tube enhances the heat transfer and friction factor by 19% and 6% compared to circular tube.	Danook et al. [12]
Elliptical tube	The elliptical tube enhances the heat transfer and friction factor by 9% and 6% compared to a circular tube.	Hussein et al. [57]

4. Zigzag Tube Design of the Heat Exchanger

Zigzag tube design of the heat exchanger, as illustrated in *Fig. 2* has become a subject of considerable interest in improving the heat transfer efficiency. Zheng et al. [58] reported an increase in heat transfer using zigzag channel with square cross-section. The zigzag geometry renders chaotic advection that brings about an increase in heat transfer rate with increasing Reynolds number [59]. The use of the zigzag channel is not limited only to normal-sized tubes. Ma et al. [60] studied the heat transfer using zigzag microchannel. It successfully reduces the growth of surface temperature and flow resistance along the direction of flow. Parlak et al. [24] numerically assessed straight, wavy, and zigzag microchannels (*Fig. 3*), wherein the Nusselt number of the wavy microchannel is 10% higher than that of the zigzag microchannel, and 40% higher than that of the straight one. Similarly, Shi et al. [61] reported an increase in the heat transfer coefficient using a square cross-section of a 2 mm wide zigzag millimetric channel with 90° bends, with a curvature radius of 1.5 mm as opposed to a straight channel. The zigzag channel model can decrease the temperature gradient on the surface of the pipe for a better heat transfer compared to a straight channel [62]. In addition, finned zigzag tube demonstrates an increase of thermal performance by 59% in laminar flow regime compared to a finned straight tube [63]. Also, Nuntadusit et al. [64] showed the optimum performance of rectangular zigzag-cut baffle against the rectangular cross-section with no cut and triangle zigzag-cut baffles at Reynolds number of 2×10^4. The upstream and downstream sides of the baffle promote the efficient transfer of heat because of flow acceleration and low friction factor. *Fig. 4* illustrates the geometry of baffles.

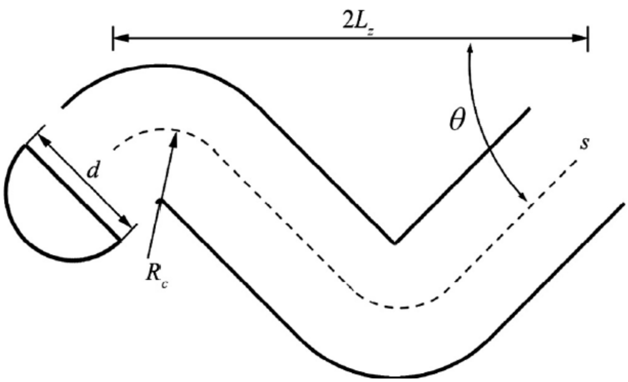

Figure 2: Schematic representation of zigzag unit with semi-circular cross-section; the dashed line represents the axial path of the passage [59]

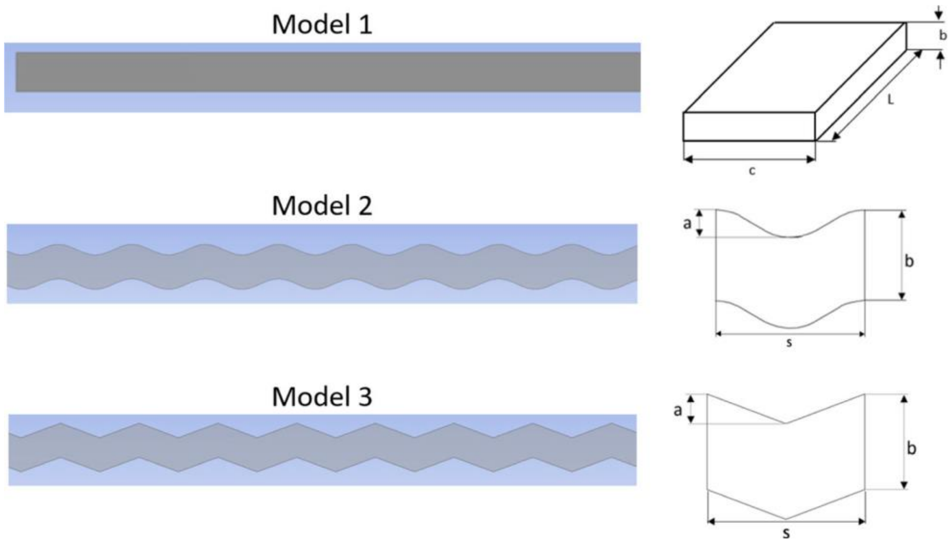

Figure 3: Straight (model 1), wavy (model 2) and zigzag (model 3) microchannels [24]

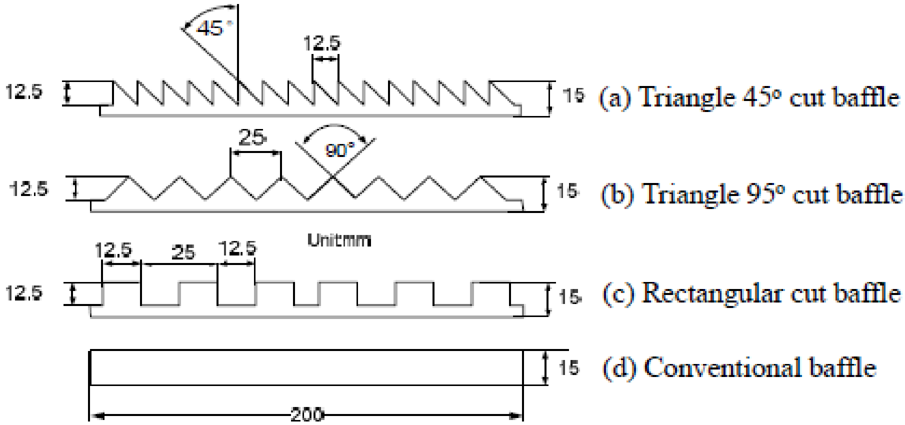

Figure 4: Geometry of baffles [64]

The use of nanofluids in zigzag channel has been reported in literature. Toghraie et al. [65] reported the heat transfer of CuO/water nanofluid in sinusoidal and zigzag-shaped microchannels, in which the Nusselt number increased by decreasing the microchannel wavelengths. Ajeel et al. [66], numerically investigated the effect of ZnO, Al_2O_3, CuO, and SiO_2 nanofluids on the heat transfer in trapezoidal-corrugated and zigzag channels. At Reynolds number of 1×10^4 to 3×10^4, the trapezoidal-corrugated channel exhibits a significant positive impact on the thermal performance and SiO_2/water shows a greater improvement in heat transfer. Table 3 summarizes the potential of zigzag tube design of heat exchangers.

Table 3: Zigzag tube design of heat exchangers

Pipe design	Finding	Reference
Zigzag channel with square cross-section	Heat transfer increases with Reynolds number, 50 < Re < 400.	Zheng et al. [58]
Zigzag channel with semi-circular cross-section	Chaotic flow advection at Re > 200 for zigzag unit geometrical parameters of R_c/d = 0.51, L_z/d = 1.75 and h = 45 mm. Heat transfer rate increases with increasing Reynolds number.	Zheng et al. [59]
Finned zigzag tube	Heat transfer increased by 59% compared to finned straight tube.	Karmo et al. [63]
Periodic zigzag channel with semi-circular cross-section	Significant increase in heat transfer with increasing Reynolds number in transient regime.	Zheng et al. [67]
Zigzag microchannel	Zigzag channel (a = 0.04 and c = 0.1) prevents the rise of heat surface	Ma et al. [60]

Pipe design	Finding	Reference
	temperature along the flow direction and reduces the flow resistance compared to rectangle channel.	
Zigzag-cut baffle, rectangular cross-section with no cut, rectangular zigzag-cut baffle, and triangle zigzag-cut baffle	The baffle with rectangular zigzag-cut gives the best thermal performance due to heat transfer augmentation in the upstream and downstream sides of the baffle.	Nuntadusit et al. [64]
Zigzag channel	The zigzag channel reduces maximum surface temperature, surface temperature difference and temperature uniformity index by 5%, 23% and 8%, respectively compared to straight channel.	Afshari et al. [62]
Sinusoidal microchannel, zigzag microchannel	Zigzag is better than sinusoidal. Nusselt number increased with increasing volume fraction of CuO and decreasing microchannel wavelengths.	Toghraie et al. [65]
Straight, wavy, and zigzag microchannels	Wavy geometry exhibits greater Nusselt number; 10% higher than zigzag, and 40% higher than straight channel.	Parlak [24]
Trapezoidal, zigzag	The symmetry of trapezoidal-corrugated channel has a great effect on heat transfer compared to zigzag and straight channels. SiO_2/water is better than other nanofluids.	Ajeel et al. [66]
Zigzag millimetric channel with square cross-section	The ratio of Nusselt number in zigzag channel to that in straight channel is always higher, increases up to 6.4 with Reynolds number.	Shi et al. [61]

5. Conclusion

This paper presents an overview of heat transfer improvement by nanofluids and zigzag tube design. The addition of nanoparticles to the basic fluids improves the heat transfer due to increase in thermal conductivity. Generally, the heat transfer can be elevated via smaller particle size and higher volumetric concentration of the nanofluid. The elliptical cross-section often exhibits a better heat transfer compared to the circular cross-section. Also, the zigzag tube design of heat exchangers leads to a better heat transfer compared to the straight tube.

Acknowledgements

This work was supported in part by UTM-ICONIC Grant No. 09G54.

References

[1] Sheikholeslami, M., Gorji-Bandpy, M., Ganji, D. D., "Review of Heat Transfer Enhancement Methods: Focus on Passive Methods using Swirl Flow Devices", *Renewable and Sustainable Energy Reviews*, Vol. 49, pp. 444–469, 2015.

[2] Kishan, R., Singh, D., Sharma, A. K., "CFD Analysis of Heat Exchanger Models Design Using ANSYS Fluent", *International Journal of Mechanical Engineering and Technology*, Vol.11, no. 2, pp. 1–9, 2020

[3] Choi, S. U., Eastman, J. A., "Enhancing Thermal Conductivity of Fluids with Nanoparticles", *International Mechanical Engineering Congress and Exhibition*, 1995.

[4] Lee, S., Choi, S. S., Li, S. A., Eastman, J. A., "Measuring Thermal Conductivity of Fluids Containing Oxide Nanoparticles", *Journal of Heat Transfer*, Vol. 121, no. 2, pp. 280–289, 1999.

[5] Sivakumar, A., Alagumurthi, N., Senthilvelan, T., "Experimental Investigation in Thermal Conductivity of CuO and Ethylene Glycol Nanofluid in a Serpentine-shaped Microchannel", *International Journal of Engineering Science and Technology*, Vol. 6, no. 7, pp. 430, 2014.

[6] Majeed, A. H., Abd, Y. H., "Performance of Heat Exchanger with Nanofluids", *Materials Science Forum*, Vol. 1021, pp. 160–170, 2021.

[7] Karimzadehkhouei, M., Sadaghiani, A. K., Motezakker, A. R., Akgönül, S., Ozbey, A., Şendur, M., Koşar, A., "Experimental and Numerical Investigation of Inlet Temperature Effect on Convective Heat Transfer of γ-Al_2O_3/Water Nanofluid Flows in Microtubes", *Heat Transfer Engineering*, Vol. 40, no. 9-10, pp. 738–752, 2019.

[8] Gheynani, A. R., Akbari, O. A., Zarringhalam, M., Shabani, G. A. S., Alnaqi, A. A., Goodarzi, M., Toghraie, D., "Investigating the Effect of Nanoparticles Diameter on Turbulent Flow and Heat Transfer Properties of Non-Newtonian Carboxymethyl Cellulose/CuO Fluid in a Microtube", *International Journal of Numerical Methods for Heat & Fluid Flow*, Vol. 29, no. 5, pp. 1699–1723, 2019.

[9] Rasheed, A. H., Alias, H., Salman, S. D., "Effects of Coil Pitch Spacing on Heat Transfer Performance of Nanofluid Turbulent Flow through Helical Microtube Heat Exchanger", *International Journal of Engineering & Technology*, Vol. 7, pp. 356–360, 2018.

[10] Wen, D., Ding, Y., "Formulation of Nanofluids for Natural Convective Heat Transfer Applications", *International Journal of Heat and Fluid Flow*, Vol. 26, no. 6, pp. 855–864, 2005.

[11] Kumar, P., "A CFD Study of Heat Transfer Enhancement in Pipe Flow with Al_2O_3 Nanofluid", *International Journal of Mechanical and Mechatronics Engineering*, Vol. 5, no. 9, pp. 1843–1847, 2011.

[12] Danook, S. H., Jasim, Q. K., Hussein, A. M., "Nanofluid Convective Heat Transfer Enhancement Elliptical Tube inside the Circular Tube under Turbulent Flow", *Mathematical and Computational Applications*, Vol. 23, no. 4, pp. 78, 2018.

[13] Madhesh, D., Kalaiselvam, S., "Experimental Study on the Heat Transfer and Flow Properties of Ag–Ethylene Glycol Nanofluid as a Coolant", *Heat and Mass Transfer*, Vol. 50, no. 11, pp. 1597–1607, 2014.
[14] Fule, P. J., Bhanvase, B. A., Sonawane, S. H., "Experimental Investigation of Heat Transfer Enhancement in Helical Coil Heat Exchangers using Water-based CuO Nanofluid", *Advanced Powder Technology*, Vol. 28, no. 9, pp. 2288–2294, 2017.
[15] Doshmanziari, F. I., Zohir, A., Kharvani, H. R., Jalali-Vahid, D., Kadivar, M., "Characteristics of Heat Transfer and Flow of Aluminum Oxide/Water Nanofluid in a Spiral-Coil Tube for Turbulent Pulsating Flow", *Heat and Mass Transfer*, Vol. 52, no. 7, pp. 1305–1320, 2016.
[16] Qi, C., Yang, L., Chen, T., Rao, Z., "Experimental Study on Thermo-Hydraulic Performances of TiO_2-H_2O Nanofluids in a Horizontal Elliptical Tube", *Applied Thermal Engineering*, Vol. 129, pp. 1315–1324, 2018.
[17] Fabbri, G., "Optimum Profiles for Asymmetrical Longitudinal Fins in Cylindrical Ducts", *International Journal of Heat and Mass Transfer*, Vol. 42, no. 3, pp. 511–523, 1999.
[18] Ouzzane, M., Galanis, N., "Numerical Analysis of Mixed Convection in Inclined Tubes with External Longitudinal Fins", *Solar Energy*, Vol. 71, no. 3, pp. 199-211, 2001.
[19] Barba, A., Rainieri, S., Spiga, M., "Heat Transfer Enhancement in a Corrugated Tube", *International Communications in Heat and Mass Transfer*, Vol. 29, no. 3, pp. 313–322, 2002.
[20] Muzychka, Y. S., Yovanovich, M. M., "Laminar Forced Convection Heat Transfer in the Combined Entry Region of Non-Circular Ducts", *Journal of Heat Transfer*, Vol. 126, no. 1, pp. 54–61, 2004.
[21] Jarungthammachote, S., "Entropy Generation Analysis for Fully Developed Laminar Convection in Hexagonal Duct Subjected to Constant Heat Flux", *Energy*, Vol. 35, no. 12, pp. 5374–5379, 2010.
[22] Schenk, J., Han, B. S., "Heat Transfer from Laminar Flow in Ducts with Elliptic Cross-Section", *Applied Scientific Research*, Vol. 17, no. 2, pp. 96–114, 1967.
[23] Rao, S. S., Ramacharyulu, N. C. P., Krishnamurty, V. V. G., Laminar Forced Convection in Elliptic Ducts", *Applied Scientific Research*, Vol. 21, no. 1, pp. 185–193, 1969.
[24] Parlak, Z., "Optimal Design of Wavy Microchannel and Comparison of Heat Transfer Characteristics with Zigzag and Straight Geometries", *Heat and Mass Transfer*, Vol. 54, no. 11, pp. 3317–3328, 2018.
[25] Rao, G. S., Sharma, K. V., Chary, S. P., Bakar, R. A., Rahman, M. M., Kadirgama, K., Noor, M. M., "Experimental Study on Heat Transfer Coefficient and Friction Factor of Al_2O_3 Nanofluid in a Packed Bed Column", *Journal of Mechanical Engineering and Sciences*, Vol. 1, no. 1, pp. 1–15, 2011.
[26] Maiga, S. E. B., Palm, S. J., Nguyen, C. T., Roy, G., Galanis, N., "Heat Transfer Enhancement by using Nanofluids in Forced Convection Flows", *International Journal of Heat and Fluid Flow*, Vol. 26, no. 4, pp. 530–546, 2005.
[27] You, S. M., Kim, J. H., Kim, K. H., "Effect of Nanoparticles on Critical Heat Flux of Water in Pool Boiling Heat Transfer", *Applied Physics Letters*, Vol. 83, no. 16, pp. 3374–3376, 2003.
[28] Sardarabadi, M., Passandideh-Fard, M., "Experimental and Numerical Study of Metal-Oxides/Water Nanofluids as a Coolant in Photovoltaic Thermal Systems (PVT)", *Solar Energy Materials and Solar Cells*, Vol. 157, pp. 533–542, 2016.
[29] Chamsa-Ard, W., Brundavanam, S., Fung, C. C., Fawcett, D., Poinern, G., "Nanofluid Types, Their Synthesis, Properties, and Incorporation Indirect Solar Thermal Collectors: A Review", *Nanomaterials*, Vol. 7, no. 6, pp. 131, 2017.

[30] Ali, H. M., Ali, H., Liaquat, H., Maqsood, H. T. B., Nadir, M. A., "Experimental Investigation of Convective Heat Transfer Augmentation for Car Radiator using ZnO–Water Nanofluids", *Energy*, Vol. 84, pp. 317–324, 2015.
[31] Hussein, A. M., Bakar, R. A., Kadirgama, K., "Study of Forced Convection Nanofluid Heat Transfer in the Automotive Cooling System", *Case Studies in Thermal Engineering*, Vol. 2, pp. 50–61, 2014.
[32] Rasheed, A. H., Alias, H. B., Salman, S. D., "Experimental and Numerical Investigations of Heat Transfer Enhancement in Shell and Helically Microtube Heat Exchanger using Nanofluids", *International Journal of Thermal Sciences*, Vol. 159, pp. 106547, 2021.
[33] Ahmed, W., Chowdhury, Z. Z., Kazi, S. N., Johan, M. R., Akram, N., Oon, C. S., "Effect of ZnO-Water-Based Nanofluids from Sonochemical Synthesis Method on Heat Transfer in a Circular Flow Passage", *International Communications in Heat and Mass Transfer*, Vol. 114, pp. 104591, 2020.
[34] Safir, N. H, Bin-Abdun, N. A., Razlin, Z. M., Amin, N. A. M., Voon, C. H., "Enhancement of Heat Transfer Properties for ZnO/Water Nanofluid in Heat Exchange Applications", *AIP Conference Proceedings*, Vol. 2030, pp. 020010, 2018.
[35] Lahari, M. L. R. C., Sai, P. H. V. S. T., Swamy, K. S. N., Murthy, N. K., Sharma, K. V., "Investigation on Heat Transfer Properties of Water Based TiO_2-ZnO Nanofluids", *Materials Science and Engineering*, Vol. 455, pp. 012092, 2018.
[36] Shahrul, I. M., Mahbubul, I. M., Saidur, R., Sabri, M. F. M., "Experimental Investigation on Al_2O_3–W, SiO_2–W and ZnO–W Nanofluids and Their Application in a Shell and Tube Heat Exchanger", *International Journal of Heat and Mass Transfer*, Vol. 97, pp. 547–558, 2016.
[37] Ali, H. M., Ali, H., Liaquat, H., Maqsood, H. T. B., Nadir, M. N., "Experimental Investigation of Convective Heat Transfer Augmentation for Car Radiator using ZnO–Water Nanofluids", *Energy*, Vol. 84, pp. 317–324, 2015.
[38] Noorbakhsh, M., Ajarostaghi, S. S. M., Zaboli, M., Kiani, B., "Thermal Analysis of Nanofluids Flows in a Double Pipe Heat Exchanger with Twisted Tapes Insert on Both Sides", *Journal of Thermal Analysis and Calorimetry*, pp. 1–12, 2021.
[39] Namburu, P. K., Das, D. K., Tanguturi, K. M., Vajjha, R. S., "Numerical Study of Turbulent Flow and Heat Transfer Characteristics of Nanofluids Considering Variable Properties", *International Journal of Thermal Sciences*, Vol. 48, no. 2, pp. 290–302, 2009.
[40] Rudyak, V. Y., Minakov, A. V., "Thermophysical Properties of Nanofluids", *Eur. Phys. J.*, Vol. 41, pp. 15, 2018.
[41] Nguyen, C. T., Desgranges, F., Roy, G., Galanis, N., Maré, T., Boucher, S., Mintsa, H. A., "Temperature and Particle-size Dependent Viscosity Data for Water-Based Nanofluids–Hysteresis Phenomenon", *International Journal of Heat and Fluid Flow*, Vol. 28, no. 6, pp. 1492–1506, 2007.
[42] Lu, W. Q., Fan, Q. M., "Study for the Particle's Scale Effect on Some Thermophysical Properties of Nanofluids by a Simplified Molecular Dynamics Method", *Engineering Analysis with Boundary Elements*, Vol. 32, no. 4, pp. 282–289, 2008.
[43] Pastoriza-Gallego, M. J., Casanova, C., Legido, J. A., Piñeiro, M. M., "CuO in Water Nanofluid: Influence of Particle Size and Polydispersity on Volumetric Behavior and Viscosity", *Fluid Phase Equilibria*, Vol. 300, no. 1-2, pp. 188–196, 2011.
[44] Eastman, J. A., Choi, S. U. S., Li, S., Yu, W., Thompson, L. J., "Anomalously Increased Effective Thermal Conductivities of Ethylene Glycol-Based Nanofluids Containing Copper Nanoparticles", *Applied Physics Letters*, Vol. 78, no. 6, pp. 718–720., 2001
[45] Chon, C. H., Kihm, K. D., Lee, S. P., Choi, S. U., "Empirical Correlation Finding the Role of Temperature and Particle Size for Nanofluid (Al_2O_3) Thermal Conductivity Enhancement", *Applied Physics Letters*, Vol. 87, no. 15, pp. 153107, 2005.

[46] Karthikeyan, N., Philip, J., Raj, B., "Effect of Clustering on the Thermal Conductivity of Nanofluids", *Materials Chemistry and Physics*, Vol. 109, no. 1, pp. 50−55, 2008.

[47] Beck, M. P., Yuan, Y., Warrier, P., Teja, A. S., "The Effect of Particle Size on the Thermal Conductivity of Alumina Nanofluids", *Journal of Nanoparticle Research*, Vol. 11, no. 5, pp. 1129−1136, 2009.

[48] Yeganeh, M., Shahtahmasebi, N., Kompany, A., Goharshadi, E., Youssefi, A., Šiller, L., "Volume Fraction and Temperature Variations of the Effective Thermal Conductivity of Nanodiamond Fluids in Deionized Water", International Journal of Heat and Mass Transfer, Vol. 53, pp. 3186−3192, 2010.

[49] Sundar, L. S., Singh, M. K., Sousa, A. C., "Investigation of Thermal Conductivity and Viscosity of Fe_3O_4 Nanofluid for Heat Transfer Applications", *International Communications in Heat and Mass Transfer*, Vol. 44, pp. 7−14, 2013.

[50] Li, C. H., Peterson, G. P., "Experimental Investigation of Temperature and Volume Fraction Variations on the Effective Thermal Conductivity of Nanoparticle Suspensions (Nanofluids)", *Journal of Applied Physics,* Vol. 99, pp. 084314, 2006.

[51] Pryazhnikov, M., Minakov, A., Rudyak, V., Guzei, D., "Thermal Conductivity Measurements of Nanofluids", *International Journal of Heat and Mass Transfer,* Vol. 104, pp. 1275−1282, 2017.

[52] Alias, H., Rasheed, A. H., Salman, S. D., "Enhancement of Nanofluid Heat Transfer in Elliptical Pipe and Helical Micro Tube Heat Exchanger", *Journal of Advanced Research in Fluid Mechanics and Thermal Sciences*, Vol. 66, no. 1, pp. 53–63, 2020.

[53] Ahmadi, K., Khanmohammadi, S., Khanmohammadi, S., Bahiraei, M., Bach, Q. V., "Heat Transfer Assessment of Turbulent Nanofluid Flow in a Circular Pipe Fitted with Elliptical-cut Twisted Tape Inserts", *Journal of Thermal Analysis and Calorimetry*, pp. 1−14, 2020.

[54] Qi, C., Chen, T., Wang, Y., Yang, L., "Experimental Study on the Thermo-Hydraulic Performance of Nanofluids in Diverse Axial Ratio Elliptical Tubes with a Built-in Turbulator", *Korean Journal of Chemical Engineering*, Vol. 37, no. 9, pp. 1466-1481, 2020.

[55] Chaurasia, P., Kumar, A., Yadav, A., Rai, P. K., Kumar, V., Prasad, L., "Heat Transfer Augmentation in Automobile Radiator using Al_2O_3–Water-Based Nanofluid", *SN Applied Sciences*, Vol. 1, no. 3, pp. 1−7, 2019.

[56] Ragueb, H., Mansouri, K., "Numerical Investigation of Laminar Forced Convection for Non-Newtonian Nanofluids Flowing Inside an Elliptical Duct under Convective Boundary Condition", *International Journal of Numerical Methods for Heat & Fluid Flow*., Vol. 29, no. 1, pp. 334–364, 2019.

[57] Hussein, A. M., Bakar, R. A., Kadirgama, K., Sharma, K. V., "Heat Transfer Enhancement with the Elliptical Tube under Turbulent Flow TiO_2-Water Nanofluid", *Thermal Science*, Vol. 20, no. 1, pp. 89–97, 2016.

[58] Zheng, Z., Fletcher, D. F., Haynes, B. S., "Chaotic Advection in Steady Laminar Heat Transfer Simulations: Periodic Zigzag Channels with Square Cross-Sections", *International Journal of Heat and Mass Transfer*, Vol. 57, no. 1, pp. 274–284, 2013.

[59] Zheng, Z., Fletcher, D. F., Haynes, B. S., "Laminar Heat Transfer Simulations for Periodic Zigzag Semicircular Channels: Chaotic Advection and Geometric Effects", *International Journal of Heat and Mass Transfer*, Vol. 62, pp. 391–401, 2013.

[60] Ma, D. D., Xia, G. D., Li, Y. F., Jia, Y. T., Wang, J., "Effects of Structural Parameters on Fluid Flow and Heat Transfer Characteristics in a Microchannel with Offset Zigzag Grooves in the Sidewall", *International Journal of Heat and Mass Transfer*, Vol. 101, pp. 427–435, 2016.

[61] Shi, H., Raimondi, N. D. M., Fletcher, D. F., Cabassud, M., Gourdon, C., “Numerical Study of Heat Transfer in Square Millimetric Zigzag Channels in the Laminar Flow Regime”, *Chemical Engineering and Processing-Process Intensification*, Vol. 144, pp. 107624, 2019.
[62] Afshari, E., Ziaei-Rad, M., Dehkordi, M. M., “Numerical Investigation on a Novel Zigzag-Shaped Flow Channel Design for Cooling Plates of PEM Fuel Cells”, *Journal of the Energy Institute*, Vol. 90, no. 5, pp. 752−763, 2017.
[63] Karmo, D., Ajib, S., Al Khateeb, A., “A New Method for Designing an Effective Finned Heat Exchanger”, *Applied Thermal Engineering*, Vol. 51, no. 1−2, pp. 539−550, 2013.
[64] Nuntadusit, C., Piya, I., Wae-hayee, M., Eiamsa-ard, S., “Heat Transfer Characteristics in a Channel Fitted with Zigzag-Cut Baffles”, *Journal of Mechanical Science and Technology*, Vol. 29, no. 6, pp. 2547−2554, 2015.
[65] Toghraie, D., Abdollah, M. M. D., Pourfattah, F., Akbari, O. A., Ruhani, B., “Numerical Investigation of Flow and Heat Transfer Characteristics in Smooth, Sinusoidal, and Zigzag-Shaped Microchannel with and without Nanofluid”, *Journal of Thermal Analysis and Calorimetry*, Vol. 131, no. 2, pp. 1757−1766, 2018.
[66] Ajeel, R. K., Salim, W. I., Hasnan, K., “Thermal and Hydraulic Characteristics of Turbulent Nanofluids Flow in Trapezoidal-Corrugated Channel: Symmetry and Zigzag-Shaped”, *Case Studies in Thermal Engineering*, Vol. 12, pp. 620−635, 2018.
[67] Zheng, Z., Fletcher, D. F., Haynes, B. S., “Transient Laminar Heat Transfer Simulations in Periodic Zigzag Channels”, *International Journal of Heat and Mass Transfer*, Vol. 71, pp. 758−768, 2014.

Acta Universitatis Sapientiae
Electrical and Mechanical Engineering, 14 (2022) 28–39

DOI: 10.2478/auseme-2022-0003

Experimental Investigation on the Coating of Nickel-Base Super Alloy Using Wire Flame Spraying

Noureddine MENASRI[1], Said ZERGANE[1], Noureddine AIMEUR[1], Abdelhamid SACI[2]

[1] University Mohamed Boudiaf of M'sila, Algeria
noureddine.menasri@univ-msila.dz, http://orcid.org/0000-0002-7373-684X
said.zergane@univ-msila.dz, https://orcid.org/0000-0002-2800-6186
noureddine.aimeur@univ-msila.dz, https://orcid.org/0000-0003-0293-8417
[2]Maintenance Equipments Industrial (M.E.I) M'sila, plasma service, Algeria
hamidahmed3361@yahoo.fr

Manuscript received July 22, 2022; revised October 15, 2022

Abstract: Inconel738 is a nickel-based super alloy widely used in manufacturing gas turbines, particularly in the manufacture of blades that are in direct contact with hot gases during their operation. As a result, these blades are subjected to high temperatures, significant static and dynamic stresses, erosion and/or hot corrosion which can be very severe. The use of coatings is one of the most effective strategies to protect materials against corrosion and increase the wear resistance of materials. In this study, β-Ni-Al coatings were sprayed onto an Inconel738 substrate using a wire flame spraying process and characterization of coating has been made.

Keywords: Nickel-based super alloy, wire flame spraying, XRD diffraction, microhardness, microstructure.

1. Introduction

Gas turbines are complex machines in which mechanical and thermal effects strongly interfere, at high stress levels for long operating times. To tackle this problem, specific materials of high technological degree have been developed, capable of satisfying these extreme loading conditions, among them nickel super alloys.

Nickel super alloys have good mechanical resistance at high temperatures. The latest developments in these materials seem to indicate that the exceptional level of performance they achieve will no longer be significantly improved with new compositions.

The only limited gains that can be achieved are through the deposition of coatings. Among these, we identify thermal spraying which allows the formation of protective coatings against wear, temperature, corrosion, etc. [1-8].

Thermal spraying is a method of surface treatment by coating combining various techniques, namely oxyacetylene flame spraying [9-13], high-velocity spraying (HVOF) [14-20], electric arc spraying [21-23], atmospheric plasma spraying [24-28] and the cold spray process [29]. The different thermal spraying processes are defined mainly by the energy source used (combustion, electric discharge). The process is conditioned by thermal and/or kinetic transfers between the sprayed material and the enthalpic source used. The kinetic energy is communicated to the particle by the speed and viscosity of the projecting gas mixture. The coating construction results from the stacking of the particles on the substrate. The balance between the kinetic and thermal energy of the particles is therefore paramount to the quality of the coating. The coating is mainly characterized by the adhesion to the substrate, the porosity levels, and the oxide content. In general, the higher the particle velocity, the better the adhesion and the lower the oxide content of the coating [30].

In recent years, a lot of development and research work has been done in the field of thermal spray coating applied on nickel super alloys to improve the surface properties.

According to Sushila Rani et al. [31], a gas turbine blade failure occurs due to the combined effect of surface degradation caused by overheating, oxidation, hot corrosion, and degradation of the highly oxidized coating. M. F. O. Schiefler Filhon et al. [32] studied the influence of spraying parameters. The variation of spray parameters had a great influence on the quality of X46Cr13 stainless steel coatings. This fact could be demonstrated by the large variation obtained in terms of microstructural characteristics, mechanical properties, and corrosion performance. Xueyuan Gong et al. [33] studied the microstructure evolution of a NiAl coating and its underlying single crystal super alloy substrate by EB-PVD. The deposited NiAl coating displayed a columnar microstructure with a preferred orientation (110). Kirkendall voids were formed in the NiAl coating, indicating the different diffusion coefficients of the elements in the coating and the substrate. Equiaxed β-NiAl grains were developed in the inter-diffusion region after diffusion annealing at 1100 ° C for 10 h, which showed different orientations of crystalline grains in the coating and substrate.

M. Kopec et al. [34] concluded that the aluminized layer can significantly improve the creep performance of nickel super alloy. It has been shown that the application of such a layer can effectively protect the raw material from processes such as oxidation, hot corrosion, or wear, and thus prolong its service life. TF An [35] focused on the effect of alumina formation and transformation on the oxidation behavior of a nickel-based super alloy with an aluminide diffusion coating. This coating improved the oxidation resistance. The oxidation kinetic curve of the nickel-based super alloy at 1000°C was slightly higher than that at 1050°C within the first 100 hours. This abnormal phenomenon is attributed to the high amount of W and Mo (about 12%). The growth stress was characterized by the formation of convoluted scales.

The β-NiAl coatings have been widely used as metal protector coatings to protect the underlying super alloy from high-temperature oxidation. D.B. Miracle [36] presented a critical review of the physical and mechanical properties of NiAl.

2. Materials and Experimental Procedures

2.1. Materials Used

The substrate used in our study is the nickel-based super alloy / Inconel 738 which is used for the manufacture of the moving blade of a gas turbine, where the detection of the chemical composition of Inconel 738 has been made by using a portable analysis device Thermo scientific NitonXL 3t. The chemical composition is shown in Table 1.

Table 1: Chemical composition of Inconel738(%weight)

	Se	Mo	Nb	Zr	W	Cu	Ni	Co	Fe
Inconel 738	0.012	1.670	0.786	0.017	2.419	1.017	59.688	8.396	0.357
	Mn	Cr	V	Ti	Al	C	B	Ta	
Inconel 738	0.078	16.023	0.043	3.269	3.4	0.10	0.001	1.75	

The Ni-Al wire, whose chemical composition is shown in Table 2, has been sprayed onto an Inconel 738 substrate using a wire flame spraying technique.

Table 2: Chemical composition of Ni-Al wire (% weight)

Al	Si	Fe	Ni	Cu	Zr
98,034	0,641	0,727	0,351	0.215	0,032

Prior to the coating process, the substrate surface has been sandblasted with grains of sand type NK F080. The purpose of this step is to remove oxides from the surface and create a roughness profile for a good adhesion of coating.

2.2. Processes and Coating Conditions

Ni-Al layers of 3 mm thickness have been deposited on Inconel 738substrate using thermal spraying technique with Metco gun (*Fig. 1*). Oxyacetylene flame was used in the case of wire flame spraying because of the high temperatures offered by the combustion of these gases. The flame could be easily adjusted to become an oxidizing, neutral or reducing flame. A neutral flame was obtained by adjusting the acetylene flow rate. The coatings have been carried out at the Industrial Equipment Maintenance Company M'sila (MEI), Algeria.

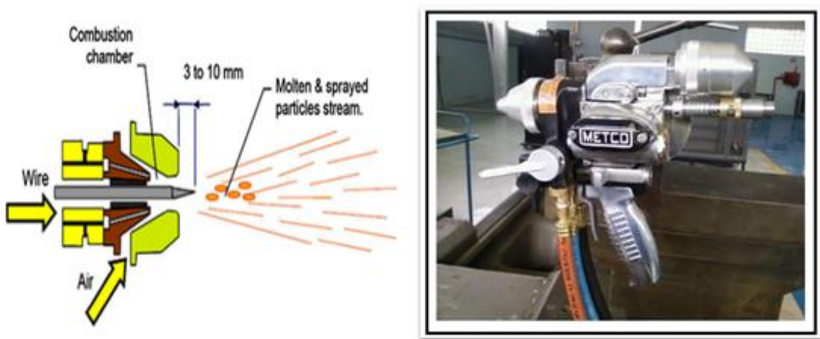

Figure 1: Operating diagram of a wire flame gun

The projection parameters are summarized in Table 3.

Table 3: Coating deposition parameters

Projection parameters	
Acetylene pressure	7 kPa
Oxygen pressure	14.7 kPa
Air pressure	33.6 kPa
Acetylene flow rate	39 L/min
Oxygen flow rate	44 L/min
Air flow rate	52 L/min
Wire diameter	3.2 mm
Spraying distance	100-200 mm
Particle velocity	150 m/s

2.3. Characterization Methods

The coated samples have been cut to a size of 15×10×2 mm^3 using a wire cutter, mounted in a cold epoxy resin, polished with abrasive papers (roughness from 200 to 5000), followed by a very fine finish polishing with an Al_2O_3 alumina powder having a grain size of 0.3μm, suspended in water on a silk cloth. Finally, the coated samples were cleaned in distilled water and dried in hot air.

Several tests were carried out in collaboration with industrial Algerian companies namely X-Ray diffraction analysis, micro hardness, and microscopic examination for the characterization of the coating.

X-ray diffraction patterns have been recorded using a PANALYTIC X'PERT PRO diffractometer equipped with a Ni filter and a copper anticathode using Kα radiation of wavelength λ = 1.5406 Å. The working conditions are: U = 30 kV and I = 25 mA, the sweep angle 2θ = 10 – 80° with a speed equal to 0.05 °/s. The samples have dimensions (10×10×2 mm^3).

Identification of the phases present in the compound has been done using micro informatics with the help of X'Pert High Score plus software (JCPDS files).

The Vickers micro-hardness measurement was performed on polished cross-sections of coatings using a Tukon Microhardness 2500 Wilson Hardness under a load of 25 g during 10 seconds. The measurement points in each zone of the section are spaced at about 0.5 mm.

The deposited coating microstructures of the cross-sections of the samples after etching in Nital 3% have been observed using optical microscopy reflection OLYMPUS BH2 in order to investigate the morphology of splatters, porosity and micro cracks [37].

3. Results and discussion

3.1. XRD Diffraction

Fig. 2 shows the X ray diffraction spectrum obtained for the (Ni-Al) coatings, performed by wire flame spraying process on an Inconel 738 substrate.

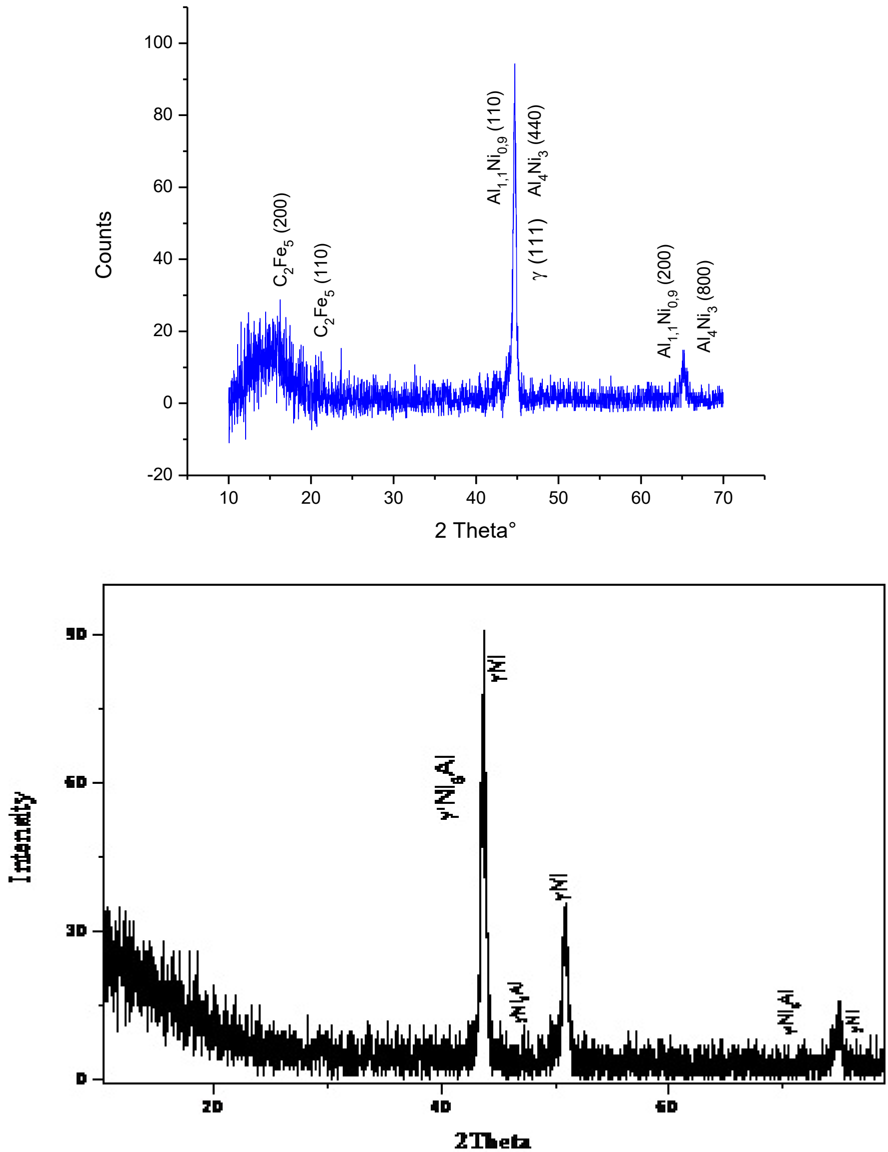

Figure 2: X ray diffraction spectra of the (Ni-Al) coating, performed by wire flame spraying process on Inconel 738 substrate

The X-ray diffraction diffractograms show the main peaks characteristic of the super alloy such as the γ matrix (JCPDS n°96-901-3033) and the γ′ precipitate phase (Ni_3Al) (JCPDS n°0021-0008). The formation of the γ′ precipitate phase is ensured by the reaction of the Nickel atoms with the Aluminum atoms of deposits. The very strong coherence between γ/γ' confers a very high hot mechanical strength of nickel-based super alloys. In addition, peaks of iron carbide (Fe_5C_2) of monoclinic crystalline structure with crystalline parameter equal to 11.5620 Å (JCPDS N° 01-089-2544) are observed. The formation of this carbide is ensured by the reaction of the iron atoms with the carbon atoms. The carbide is responsible to increase coating hardness and wear resistance.

3.2. Microhardness

Fig. 3 shows the micro hardness distribution in a cross-section of the coating obtained by flame spraying of Ni-Al wire on Inconel 738 substrate. The curve shows clearly that the coating is harder than the substrate. The nickel-aluminum alloy coating has a small variation in micro hardness from the first measuring point to the fifth point. The maximum is equal to 488HV at the 4^{rd} measurement point and the minimum is equal to307HV at the first measurement point. Micro hardness is very dependent on the nature and the distribution of the phases in the coatings-substrate. The hardness of the substrate is almost stable along the investigated area.

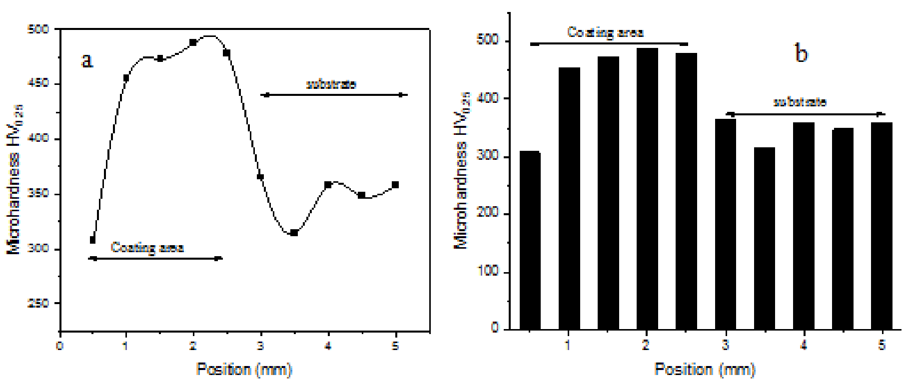

Figure 3: (a) Distribution of the Vickers micro hardness values, measured in the cross-section of the coatings / substrate domain and (b) histogram representation

3.3. Coating Microstructure

The microstructure of thermally sprayed coatings, which results from the solidification and sintering of the particles, often contains pores, oxides and cracks.

Fig. 4 shows the cross-section view of the coating wire flame spraying (Ni-Al) on substrate Inconel 738, which contains several dispersed phases: the major phase γ matrix, the γ′ precipitate phase (Ni_3Al) deformed from different directions with remarkable intensities and a small amount of carbides.

The presence of certain types of pores has been observed. The low particle velocity of the thermal spraying flame process has the effect that the certain particles are not well dispersed during the impact on the substrate. Therefore, this phenomenon favors the presence of pores in the coating. However, no crack has been revealed. The profile interface appears to adhere to the substrate.

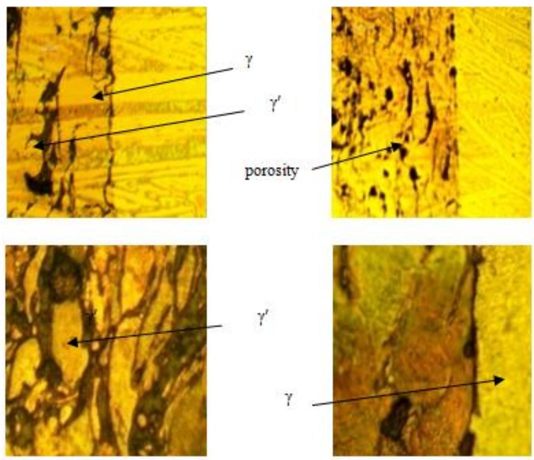

Figure 4: Optical imaging of the samples investigated by using a metallographic microscope: the selected pictures indicate the cross-section images taken from a limited area of the transition domain between Inconel super alloy substrate and the Ni-Al coating / substrate

4. Conclusion

Nickel-based alloys hardened by precipitation of the phase (γ') used in the blades of gas turbines are very complex materials. Exposed to high temperatures during service, their high temperature strength and endurance are unmatched by any class of alloy.

Improving the performance of gas turbines is an important issue, which requires identifying and understanding the deterioration mechanisms that take place during their use. In the hottest parts of gas turbines (i.e. combustion chamber), the materials used are subjected to high thermal and mechanical stresses. This is particularly the case of turbine blades. The temperatures of use are indeed, of the order of 800 °C. These stresses induce different types of degradation. The most frequently encountered by turbine blades are erosion, creep, fatigue, corrosion and oxidation.

In order to improve the high temperature durability of the turbine blades, coatings are made by thermal spraying with flame - wire (Ni-Al), deposited with the thermal spraying systems Metco.

From the characterizations by optical microscopy, micro-hardness measurements and the X-ray analysis, the following main results have been obtained:

- The presence of several distinct phases, which gives a heterogeneous structure. The phases revealed have compound, and elemental types. We can observe the presence of Ni_3Al (γ'), carbides, and the Nickel (γ) matrix.
- The adhesion of the flame wire coating is less acceptable, with the existence of pores.
- The micro hardness of the wire flame coating is higher than that of the substrate. This can be explained by the formation of the hardening phase of Ni_3Al with a significant increase of micro-hardness.
- We can confirm that wire flame spraying remains an effective solution in ordinary industrial applications where there is no high precision requirement to extend the life of the equipment without increasing the cost of the latter.

Acknowledgements

The authors would like to thank the engineers from the Maintenance Equipments Industrial (M.E.I) M'sila, Algeria and the general direction of research and development technology (DGRSDT) for their help.

References

[1] Mudgal, D., et al., "Corrosion behavior of bare, Cr3C2-25%(NiCr), and Cr3C2-25%(NiCr)+ 0.4% CeO2-coated superni 600 under molten salt at 900° C", *Journal of materials engineering and performance*, Vol. 23, no. 11, pp. 3805–3818, 2014. DOI: https://doi.org/10.1007/s11665-014-1177-3.

[2] Kumar, S., et al., "Cyclic oxidation behavior of bare and Cr3C2-25 (NiCr) coated super alloy at elevated temperature", *Adv. Mater. Lett*, Vol. 4, no. 10, pp. 754–761, 2013. DOI: https://doi.org/10.5185/amlett.2013.2428.

[3] Yang, Q., Xing, A., and Zhanqiang, L., "Machining performance and tool wear of coated carbide inserts in high speed turning powder metallurgy nickel-base superalloy", in *2010 WASE International Conference on Information Engineering*, IEEE, 2010, pp. 71–74.

[4] Mazur, Z., et al., "Failure analysis of a gas turbine blade made of Inconel 738LC alloy", *Engineering failure analysis*, Vol. 12, no. 3, pp. 474–486, 2005. DOI: https://doi.org/10.1016/j.engfailanal.2004.10.002.

[5] Li, S.-L., Qi, H.-Y., and Yang, X.-G., "Oxidation-induced damage of an uncoated and coated nickel-based superalloy under simulated gas environment", *Rare Metals*, Vol. 37, no. 3, pp. 204–209, 2018. DOI: https://doi.org/10.1007/s12598-017-0931-8.

[6] Alidokht, S. A. and Chromik, R. R., "Sliding wear behavior of cold-sprayed Ni-WC composite coatings: Influence OF WC content", *Wear*, Vol. 477, pp. 203792, 2021. DOI: https://doi.org/10.1016/j.wear.2021.203792.

[7] Gibson, G., et al., "Influence of shot peening on high-temperature corrosion and corrosion-fatigue of nickel based superalloy 720Li", *Materials at High Temperatures*, Vol. 33, no. 3, pp. 225–233, 2016, DOI: https://doi.org/10.1080/09603409.2016.1161945.

[8] Aouici, S., et al., "Corrosion Resistance of Coatings Produced by Spraying Powders Under a Laser Beam in a Saline Environment NaCl 3% by the Electrochemical Method", *Acta Universitatis Sapientiae, Electrical and Mechanical Engineering*, Vol. 12, no. 1, pp. 105–116, 2020.

[9] Rachidi, R., El Kihel, B., and Delaunois, F., "Microstructure and mechanical characterization of NiCrBSi alloy and NiCrBSi-WC composite coatings produced by flame spraying", *Materials Science and Engineering: B*, Vol. 241, pp. 13–21, 2019. DOI: https://doi.org/10.1016/j.mseb.2019.02.002.

[10] Redjdal, O., et al., "Characterization of thermal flame sprayed coatings prepared from FeCr mechanically milled powder", *Journal of Materials Processing Technology*, Vol. 213, no. 5, pp. 779-790, 2013, DOI: https://doi.org/10.1016/j.jmatprotec.2012.11.018.

[11] Amokrane, B. M., et al., "Microstructural and mechanical properties of Ni-base thermal spray coatings deposited by flame spraying", *Metallurgical and materials transactions B*, Vol. 42, no. 5, pp. 932–938, 2011, DOI: https://doi.org/10.1007/s11663-011-9551-0.

[12] Bradai, M. A., et al., "Study of microstructure, phases and microhardness of metallic coatings deposited by flame thermal spray", *Journal of Materials Processing Technology*, Vol. 200, no. 1–3, pp. 410–415, 2008, DOI: https://doi.org/10.1016/j.jmatprotec.2007.08.048.

[13] Lunn, G. D., Riley, M., and McCartney, D., "A study of wire breakup and in-flight particle behavior during wire flame spraying of aluminum", *Journal of*

Thermal Spray Technology, Vol. 26, no. 8, pp. 1947–1958, 2017, DOI: https://doi.org/10.1007/s11666-017-0639-1.

[14] Bhosale, D. G., et al., "High temperature solid particle erosion behaviour of SS 316L and thermal sprayed WC-Cr3C2–Ni coatings", *Wear*, Vol. 462, pp. 203520, 2020. DOI: https://doi.org/10.1016/j.wear.2020.203520.

[15] Liu, W.-H., Shieu, F.-S., and Hsiao, W.-T., "Enhancement of wear and corrosion resistance of iron-based hard coatings deposited by high-velocity oxygen fuel (HVOF) thermal spraying", *Surface and Coatings Technology*, Vol. 249, pp. 24–41, 2014, DOI: https://doi.org/10.1016/j.surfcoat.2014.03.041.

[16] Hardwicke, C. U. and Lau, Y.-C., "Advances in thermal spray coatings for gas turbines and energy generation: a review", *Journal of Thermal Spray Technology*, Vol. 22, no. 5, pp. 564–576, 2013, DOI: https://doi.org/10.1007/s11666-013-9904-0.

[17] Adarsha, H., et al., "Investigations on the abrasive wear behaviour of molybdenum coating on SS304 and A36 using HVOF technique", *Materials Today: Proceedings*, Vol. 5, no. 11, pp. 25667–25676, 2018, DOI: https://doi.org/10.1016/j.matpr.2018.11.008.

[18] Hong, S., et al., "Microstructure and electrochemical properties of nanostructured WC–10Co–4Cr coating prepared by HVOF spraying", *Surface and Coatings Technology*, Vol. 235, pp. 582–588, 2013, DOI: https://doi.org/10.1016/j.surfcoat. 2013.08.029.

[19] Szymański, K., et al., "Thermally sprayed coatings resistant to erosion and corrosion for power plant boilers-A review", *Surface and Coatings Technology*, Vol. 268, pp. 153–164, 2015, DOI: https://doi.org/10.1016/j.surfcoat.2014.10.046.

[20] Patil, V., et al., "High Temperature Corrosion Behavior of High Velocity Oxy Fuel Sprayed NiCrMoFeCoAl-30% SiO2 and NiCrMoFeCoAl-30% Cr2O3 Composite Coatings on ASTM SA213-T22 Steel in a Coal-fired Boiler Environment", *International Journal of Engineering: Transactions A: Basics*, Vol. 35, no. 7, pp. 1416-1427, DOI: https://doi.org/10.5829/ije.2022.35.07a.19.

[21] Kumar, D., Murtaza, Q., and Singh, R., "Sliding wear behavior of aluminum alloy coating prepared by two-wire electric arc spray process", *The International Journal of Advanced Manufacturing Technology*, Vol. 85, no. 1, pp. 237–252, 2016, DOI: https://doi.org/10.1007/s00170-015-7920-6.

[22] Lima, C., et al., "Assessment of abrasive wear of nanostructured WC-Co and Fe-based coatings applied by HP-hVOF, flame, and wire arc spray", *Journal of Thermal Spray Technology*, Vol. 23, no. 7, pp. 1097–1104, 2014, DOI: https://doi.org/10.1007/s11666-014-0101-6.

[23] Kumar, S., Kumar, M., and Handa, A., "Comparative study of high temperature oxidation behavior and mechanical properties of wire arc sprayed NiCr and NiAl coatings", *Engineering failure analysis*, Vol. 106, pp. 104173, 2019, DOI: https://doi.org/10.1007/s11666-014-0101-6.

[24] Yang, Q., Zhao, L., and Patnaik, P., "Erosion performance, corrosion characteristics and hydrophobicity of nanolayered and multilayered metal nitride coatings", *Surface and Coatings Technology*, Vol. 375, pp. 763-772, 2019, DOI: https://doi.org/10.1016/j.surfcoat.2019.07.074.

[25] Kumar, R. and Kumar, S., “Thermal Spray Coating: A Study”, *International Journal Of Engineering Sciences & Research Technology*, Vol. 7, no. 3, pp. 610–617. DOI: https://doi.org/10.5281/zenodo.1207005.

[26] Pattankude, B. G. and Balwan, A., “A Review On Coating Process”, *International Research Journal of Engineering and Technology*, Vol. 6, no. 3, pp. 7980–7984, 2019.

[27] Poursaeidi, E., Torkashvand, K., and Mohammadi, M., “Air Plasma Sprayed Bond Coat Oxidation Behavior and its Resistance to Isothermal and Thermal Shock Loading”, *International Journal Of Engineering. Transactions C: Aspects*, Vol. 32, no. 6, pp. 872–876, 2019, DOI: https://doi.org/10.5829/ije.2019.32.06c.11.

[28] Thiem, P., et al., “Comparison of microstructure and adhesion strength of plasma, flame and high velocity oxy-fuel sprayed coatings from an iron aluminide powder”, *Surface and Coatings Technology*, Vol. 324, pp. 498–508, 2017, DOI: https://doi.org/10.1016/j.surfcoat.2017.06.016.

[29] Goldbaum, D., et al., Review on cold spray process and technology US patents, in *Modern Cold Spray*, *Springer*, pp. 403–429. 2015.

[30] Suo, X., et al., “Preparation and characterization of magnesium coating deposited by cold spraying”, *Journal of Materials Processing Technology*, Vol. 212, no. 1, pp. 100-105, 2012, DOI: https://doi.org/10.1016/j.jmatprotec.2011.08.010.

[31] Rani, S., Agrawal, A. K., and Rastogi, V., “Failure analysis of a first stage IN738 gas turbine blade tip cracking in a thermal power plant”, *Case studies in engineering failure analysis*, Vol. 8, pp. 1–10, 2017, DOI: https://doi.org/10.1016/j.csefa.2016.11.002.

[32] Schiefler Filho, M., et al., “Influence of process parameters on the quality of thermally sprayed X46Cr13 stainless steel coatings”, *Journal of the brazilian society of mechanical sciences and engineering*, Vol. 26, no. 1, pp. 98–106, 2004.

[33] Gong, X., et al., “Microstructure evolution of an EB-PVD NiAl coating and its underlying single crystal superalloy substrate”, *Journal of Alloys and Compounds*, Vol. 672, pp. 36-44, 2016, DOI: https://doi.org/10.1016/j.jallcom.2016.02.115.

[34] Kopec, M., et al., “Aluminide thermal barrier coating for high temperature performance of MAR 247 nickel based superalloy”, *Coatings*, Vol. 11, no. 1, pp. 48, 2021, DOI: https://doi.org/10.3390/coatings11010048.

[35] An, T. F., et al., “Effect of the Al2O3 transformation in scales on the oxidation behavior of a nickel-base superalloy with an aluminide diffusion coating”, *Oxid Met*, Vol. 54, no. 3/4, pp. 301–316, 2000, DOI: https://doi.org/10.1023/A:1004654429687.

[36] Miracle, D., “Overview No. 104 The physical and mechanical properties of NiAl”, *Acta metallurgica et materialia*, Vol. 41, no. 3, pp. 649-684, 1993, DOI: https://doi.org/10.1016/0956-7151(93)90001-9

[37] Hesari, F., Moradi, M., and Torknik, F., “Transmission Electron Microscopy Sample Preparation of INCONEL 738 Nickel-Base Superalloy”, *International Journal of Engineering*, Vol. 32, no. 6, pp. 852–859, 2019, DOI: https://doi.org/10.5829/ije.2019.32.06c.08.

Acta Universitatis Sapientiae
Electrical and Mechanical Engineering, 14 (2022) 40–49

DOI: 10.2478/auseme-2022-0004

Control of Remote Robots by Means of Cell Phones

Abdelouahab ZAATRI[1], Ridha KELAIAIA[2]

[1] Department of Mechanical Engineering, University of Constantine1, Constantine, Algeria, e-mail: zaatri@hotmail.com
[2] LGMM Laboratory, Faculty of Technology, University of 20 August 1955-Skikda, PB N° 26 Route Elhadaik, Skikda 21000, Algeria, e-mail: r.kelaiaia@univ-skikda.dz

Manuscript received May 24, 2022; revised September 03, 2022

Abstract: Since about two decades, cellular phones coupled to internet and wireless communications are offering many possibilities that can be exploited by classical telerobotics to free human operators from many constraints providing mobility and ubiquitous applications.

This paper presents the design and implementation of an experimental telerobotics system where the human operator supervises and controls remote robots by means of cell phones. To achieve this application, we used Java software namely J2ME platform which is dedicated for programming cell phones and J2SE platform for programming PCs. The adopted software technology of connection between the human operator and the remote robots uses the socket technique with client-server model. The cell phone held by the operator acts as a Client while a PC, situated at the remote robot site, acts as a Server. This application corresponds to Midlet-to-Servlet in Java terminology. Basic simulations and preliminary experiments have been successfully carried out with a three Degrees-of-Freedom (D.O.F) serial robot. These telerobotics systems based on cell phones are effectively offering interesting means to opening new perspectives for mobile and ubiquitous applications.

Keywords: Telerobotics, human-robot interaction, cell phone control, wireless control, remote control, client-server architecture.

1. Introduction

Since about three decades, the evolution of modern technology is offering more and more capabilities to enable mobile interaction and control of remote systems in an easy way anywhere at any time [1-4]. Initially, remote robot control took form during the Second World War by controlling the first robot manipulators dedicated to manipulate radioactive materials in nuclear plants and to achieve repetitive industrial tasks. During this period, the feedback information used to monitor and supervise the task was the direct vision of human operators situated near the operational site. Later on, remote robot control or telerobotics became possible at relatively longer distances with dedicated and specialized wired or wireless connections based on radio waves. For supervising and controlling tasks at long distances, the vision feedback is assured by means of cameras situated at the remote robot site. Soon, this field of telerobotics became very important and involved various kind of robots: arm manipulators, wheeled robots [5], parallel robots [6], etc. It covered also a large number of applications including exploration in hazardous and/or inhabited areas like space, undersea, nuclear plants. However, since the 90's, the availability of multimedia techniques has enriched the development of operator interfaces which represent the core of telerobotics systems. Interaction, control and supervision of telerobotics systems became therefore easier [7-10]. More recently, the involvement of Artificial Intelligence into telerobotics brought unexpected and unprecedented capabilities which are reflected by the addition of more autonomy and flexibility to the telerobotics systems. Consequently, more and new applications have been carried out such as telemedicine, tele-surgery, micro-robotics, social robotics, cooperative robotics, etc. Many complex missions involving various robots of different forms and sizes are actually envisioned [11]. In fact, the standard basic architecture of telerobotics systems is usually constituted of three main parts. The first part is a local site where the human operator is situated and from where usually he/she interacts and supervises the remote robot. The second part is the remote site where the robot is situated in its workspace. The third part is an operator interface which permits communication between the operator on the one hand, and the remote robot and its environment on the other hand. An operator interface is generally constituted of screens projecting the scene of the robot evolving in its workspace and many tools that enable the operator to interact and supervise the task achievement and the robot state. Classically, the local site is fixed and the remote robot can be mobile or spatially fixed according to the robot type under consideration. However, with the recent development of modern wireless communication networks involving Internet; cell phones as handheld devices are becoming to some extent capable of replacing PCs. This capability, if exploited in telerobotics, can give rise to applications implying free displacements of the operator. This is particularly required for human explorers, soldiers, and many others. Indeed, cell phones enable unimaginable means for remote control which can be characterized by the ease of use anywhere and at any time. If the human operators are mobile and the remote robot systems are also mobile; therefore, ubiquitous applications can be designed.

In this context, some studies and applications have been performed covering a large spectrum of domains: education, academic [3] surveillance [12, 13], spying [14], control of mobile robots [4], [15], industrial robots [16], military operations [17], supervision of unmanned vehicles [18], exploratory missions in space and hazardous environments, etc. [4].

In this paper, we intend to present the design and implementation of an experimental telerobotics system in which the human operator can control and supervise remote robots by means of cell phones of the third generation and beyond, using wireless networks.

2. Description of the Telerobotics System Based on Cell Phones

A. Hardware Architecture Design

The hardware architecture of our telerobotics system resembles to classical ones except that the operator can be mobile according to his/her needs. A schematic illustration of the system organization is presented in *Fig. 1*. It is composed of three main parts. The first part concerns the local site where stands the human operator, who can supervise and control by means of the cell phone the remote robot as well as the webcam (on the right side of *Fig.1*). The second one is constituted by the remote worksite (on the right side). It contains a homemade 3 D.O.F robot manipulator of RRR type that holds a gripper on its end-effector. In addition, this site contains a homemade pan-tilt unit that serves to orient a webcam used for selecting views on the robot workspace.

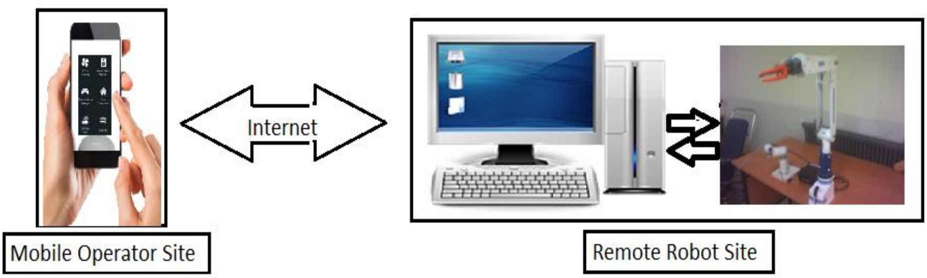

Figure 1: Hardware architecture with operator using cell phone

The third part concerns the communication and control system which enables information exchange and interactions between the human operator and the remote robot and site. The required functions of our system are hosted on the cell phone through a Graphical User Interface (GUI). The GUI permits management of information exchange and visualization of the remote site on the cell phone. It provides functions via panels for remotely controlling the robot manipulator for performing tasks as well as the pan tilt unit for selecting suitable views by the webcam.

The vision feedback to supervise the remote task is assured by video streams sent by the camera and displayed on the screen of the cell phone. Moreover, a virtual robot replicating the wireframe structure of the real robot has been also designed and implemented for simulation purposes based on the cell phone emulator.

B. Software Architecture Design

Our application has been designed for modern cell phones of the third generation and beyond using wireless networks such as WWAN (Wireless Wide Area Network) and thus can take advantage of the access to Internet and multimedia systems. In our telerobotics system, the mobile terminals are connected to the wireless network. Therefore, it was necessary to use specific software for developing mobile phone applications. Consequently, we have used the basic J2ME platform which is a specific platform dedicated to mobile phone applications [19-21].

Applications concerning virtual as well as real robots have been designed by means of this platform. The communication between the mobile phone and the PC at the remote robot site exploits the socket technology according to the well-known Client-Server model. The Client represents the operator's cell phone while the Server is represented by a PC related to the remote site. The dialogue between the Client and the Server is done by exchanging messages. As we have used Java software platforms to implement all our applications; so, we have implemented a MIDlet class for the Client side and the Servlet class for the Server side [22]. A MIDlet is an application that uses the mobile information device profile (MIDP) from the Java Platform Micro Edition (Java ME) environment. Since Java has become one of the most widely used mobile platform, the MIDlet has become the most ubiquitous application of mobile ones. On the other hand, a Servlet is a class that is used to extend the capabilities of servers that host applications accessible by means of a request-response programming model. This Java platform offers also a cell phone emulator on PCs. This is an important facility that enables programming and testing applications designed for cell phones on the PCs.

The GUI has been designed to enable interaction and information exchange between the human operator and the remote site. Technically, the GUI provides the operator with a menu on the cell phone from which he/she can select functions to be performed. It is constituted of some forms that integrate buttons, labels, zones to input data, zones to receive messages, etc. For instance, a specific panel is designed to control the orientation of the webcam by pen clicks or finger touches or by predefined programs. An area is devoted to visualize the video sent by the webcam from the remote site. This enables to supervise the accomplishment of the remote task. Another panel can be used for controlling the robot movement of the serial robot from one configuration to the next. From this panel, the operator can also launch preprogrammed simple pick-and-place tasks.

3. Functional Organization of the Telerobotics System

In this section, we briefly present the functional organization of our telerobotics system. All communications and interaction between these two sites are managed through the structure of client-server model (MIDlet-to-Servlet). Expressed in hardware terms, it means that all communications are performed between the cell phone and the PC. The process of communication between the Midlet and the Servlet works as follows (*Fig. 2*). When the operator needs to interact with the remote site, he/she activates by a pen or a finger touch a button of an appropriate panel on the cell phone; then the Midlet invokes the Servlet. If the Server confirms by a message that it is Idle, then the operator can send the data with the service request.

For security and efficiency purposes, a procedure for error detection by simulation has been implemented [23]. This procedure necessitates a task simulation on the virtual robot before enabling real execution with the remote real robot for avoiding possible errors, non-realizable and singular configurations that can occur with some provided data. In fact, for telerobotics systems using networks such as Internet, the virtual robot is not only implemented on the cell phone at the operator site but also on the PC of the remote site. The simulation on the remote site is optionally available because it can be essentially needed in order to test and estimate the communication quality and possible issues such as micro-interruptions, delays and their random variability that can affect the network under consideration.

In practice, the operator, from the client side, formulates a request to transfer the robot from a current position to another one by sending the appropriate coordinates (x, y, z). The robot movement is simulated first with the virtual robot implemented on the client side. If this simulation fails, then an error is reported to the operator who has to cope with this situation for instance by modifying the data. In case of a successful accomplishment, the data is transmitted for simulation to the server side in order to test and estimate the influence of the network. If the simulation is performed successfully, then the execution of the task with real robot can be performed. During the real execution, a video stream is sent from the server to the client enabling the operator to supervise and control the task execution. After the effective accomplishment of the task, the server has to notify the end of the task to the client.

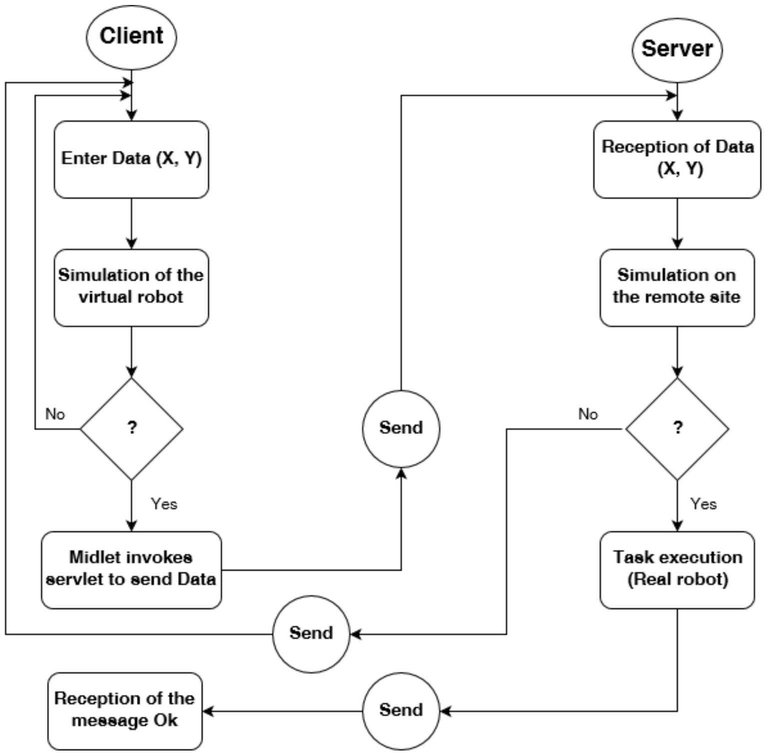

Figure 2: Functional organization scheme of the Midlet-to-Servlet communication

4. Some Simulations and Experiments

Many simulations have been performed by the virtual robot in order to test some elementary commands such as move left, move right, move up, etc. The same commands have been performed with the real robot. Some simple pick-and-place tasks have been also carried out by our virtual and real robots. On the other hand, different actions concerning the pan-tilt unit for orienting the camera have been also performed. *Fig. 3* shows images representing the elements that have served to perform our experiments. We can recognize from the left side to the right side: a panel showing the virtual robot used for simulation on the cell phone screen at the operator's site (*Fig. 3a*); the robot in the remote environment (*Fig. 3b*); and the pan-tilt unit holding the webcam at the remote site (*Fig. 3c*).

a.) Virtual robot b.) Serial robot c.) PTU

Figure 3: Some elements used in the experiments

Some tasks have been simulated on the virtual robot of the operator's cell phone. Other simulations have also been performed on the PC at the remote site enabling to test the quality of the communications such as the instability caused by time delays, possible micro interruption on the network and any other issues. Experiments with the real robot have been carried out only at relatively short distances in our laboratory (a few meters). The effect of the very short delays which is about milliseconds has no significant influence on the robot control compared to its effect experienced with our classical telerobotics system at distances of about 600 km. The delay is sensed particularly with manual control by joysticks or continuous finger touch on sliders of the GUI, especially if actions are complex and performed in a fast way with respect to relatively long delays.

Moreover, our experiments have tested commands generated by pen clicks and by impulse contact by finger touches on the cell phone screen. Since these types of commands correspond to preprogrammed short movements of the remote robot; so, they were not sensitive to delays. It reveals as in other works that interactive discrete commands enable to avoid instability and difficulty of control compared to manual control where the operator is engaged continuously to direct the remote task.

5. Conclusions and Future Work

The goal of this study was the testing of some command modes for telerobotics systems based on cell phones for providing free mobility to human operators. The adopted communication technique used the client-server model. In this model, on the one side, the operator's cell phone acts as a client while, on the other side, the PC at the remote robot site acts as a server. The technology adopted used Java platforms J2ME and J2SE corresponding to a Midlet-Servlet communication technique. This technology proves to be very easy to implement and very flexible to adapt to such telerobotics systems. The basic simulations and experiments carried out with our telerobotics system based on cell phone are offering new capabilities and opportunities for ubiquitous telerobotics applications.

As future works, there are some command modes that deserve to be tested on our telerobotics system based on cell phones. These command modes have been previously designed, implemented and successfully tested on different robots developed in our laboratory and described in the papers [24], [25]. These concerned command modes are namely interactive programming based on the graphical-user-interfaces, voice-based, pointing-on-image-based, and gesture-based [25].

Moreover, the cell-phone-based architecture can also be adapted and extended to many other robotic structures such as mobile robots, parallel robots, cable-based robots, etc.

References

[1] Álvares, A. J., and Romariz Jr, L. S. J., "Telerobotics: Methodology for the Development of a Through-the-Internet Robotic Teleoperated System", *Journal of the Brazilian Society of Mechanical Sciences,* Vol. 24, No. 2, pp. 112–126, 2002.

[2] Prashanti, B. S, Vineetha, P. S., Radhika, S., Swapna, D., Dhulipalla, D. N., "Design of GSM based wireless controlled robot", in *Proc. of the 1st International and 18th ISME Conference ISME 18*, February 23rd – 25th, 2017, NIT Warangal, Warangal, 2017, pp. 1–5.

[3] Oros, N., and. Krichmar. J. L., "Smartphone Based Robotics: Powerful, Flexible and Inexpensive Robots for Hobbyists, Educators, Students and Researchers", *CECS Technical Report* 13-16 November 26, Center for Embedded Computer Systems University of California, Irvine, 2013.

[4] Boboc, R. G., Horatiu, M., and Talaba, D., "A Review of Current Applications in Teleoperation of Mobile Robots", *Bulletin of the Transilvania University of Braşov, Series I: Engineering Sciences*, Vol. 5 (54), No. 2., 2012, pp. 9–16.

[5] Bouzoualegh, S., Guechi, E.-H. and Kelaiaia, R., "Model Predictive Control of a Differential-Drive Mobile Robot", *Acta Universitatis Sapientiae, Electrical and Mechanical Engineering*, Vol. 10, No.1, 2018, pp. 20–41, https://doi.org/10.2478/auseme-2018-0002.

[6] Brahmia, A., Kelaiaia, R., Chemori, A., and Company, O., "On Robust Mechanical Design of a PAR2 Delta-Like Parallel Kinematic Manipulator", *ASME. J. Mechanisms Robotics*, February 2022; 14(1): 011001, https://doi.org/10.1115/1.4051360.

[7] Zaatri, A., Oussalah, M., "Integration and design of multi-modal interfaces for supervisory control systems", *Information Fusion*, Vol. 4, Issue 2, pp. 135–150, 2003.

[8] Zendoui, F. Z., Mahmoudi, M., Zaatri, A., "Development and Experimentation of an Articulated Mechanical System using Internet", *Mechanica*, Vol. 24 (4), pp. 462–466, 2018.

[9] Qamar, I., Shubam, S., Dikshit, L., Faiza, T., Ishrat, N., "Cell Phone Controlled Robotic Vehicle", *International Journal of Scientific Research in Computer Science, Engineering and Information Technology*, Vol. 4, Issue 1, 2018.

[10] Montúfar-Chaveznava, R., Paisano, C., and Cañas, J. M., "Simulating Telerobotics by Cellular Telephony", in *Proceedings of the Second International Conference on Informatics in Control, Automation and Robotics - Robotics and Automation*, pp. 329–334, 2005.

[11] Gonde, D., Jadhav, S., Lokhande, M., "Robot Control using Android Smartphone", *Journal of Android and IOS Applications and Testing*, Vol. 1(1), pp. 1–5, 2016.

[12] Selvam1, M., "Smart Phone Based Robotic Control for Surveillance Applications", *IJRET: International Journal of Research in Engineering and Technology*, Vol. 03, Issue 03, pp. 229–232, 2014.

[13] Arora, L., and Joglekar, A., "Cell Phone Controlled Robot with Fire Detection Sensors", *(IJCSIT) International Journal of Computer Science and Information Technologies*, Vol. 6 (3), pp. 2954–2958, 2015.

[14] Hasan, A. S., Jewel, M. K. H., Mostakim, M. N., Bhuiyan, N. H., Rahman, M., Hossain, S. D. and Khalid Hossain, M., "Smartphone Controlled Spy Robot with Video Transmission and Object Collector", *International Journal of Engineering and Manufacturing*, Vol. 7, pp. 50–58, 2017.

[15] Aruna, D. and Bharathi, R., "Robot control using mobile phone", *International Journal of Electrical and Electronics Engineers*, Vol. 7, No. 2, pp. 61-68, 2015.

[16] Ahmed, M, and Pathan J. K., "3 G based industrial automation using GSM communication", *International Journal of Research in Environmental Science and Technology*, Vol. 1, No. 1, pp 16–21, 2011.

[17] Patel, J., Malik, A., Thakare, V., Rajput, R., "War Field Robot Controlled by Android Phone", *International Journal of Innovative Research in Computer and Communication Engineering*, Vol. 3, Issue 1, 2015.

[18] Acharya, C.M., and Vedvyas, D., "Design and Development of a GSM Controlled Unmanned Ground Surveillance Vehicle (v1.0)", *International Journal of Computer and Electronics Engineering*, Vol. 4, No. 1, pp. 13–24, 2012.

[19] Piroumian, V., "Wireless J2ME Platform Programming", *Sun microsystems press and prentice hall*, 2002.

[20] Vazquez-Briseno, M., Vincent, P., Nieto-Hipolito, J. I., et al., "Applying a Modular Framework to Develop Mobile Applications and Services", *Journal of Universal Computer Science*, Vol. 18, no. 5, pp. 704–727, 2012.

[21] Chakravorty, R., Banerjee, S., Rodriguez, P., et al., "Performance optimizations for wireless wide-area networks: Comparative study and experimental evaluation", in *Proc. ACM Mobicom*, 2004. pp. 159–173.

[22] http://Java.sun.com/products/servlet/

[23] Zaatri, A., and Van Brussel, H., “Error detection by anticipation for vision-based control”, *Sciences & Technologie A, Sciences Exactes*, (15), pp. 83–89, 2001.
[24] Zaatri, A., “Investigations into integrated supervisory control systems. Doctoral Thesis”, Katholieke Universiteit, Leuven, Belgium, 2000.
[25] Zaatri, A., “Overview of some Command Modes for Human-Robot Interaction Systems”, *Journal of Information Systems Engineering and Management*, Vol. 7, N.2, 2022.

Acta Universitatis Sapientiae
Electrical and Mechanical Engineering, 14 (2022) 50–64

DOI: 10.2478/auseme-2022-0005

Optimal Power Sharing Control of the Hybrid Energy Storage System of an Electric Vehicle Along a Standard Driving Cycle

János FERENCZ[1], András KELEMEN[2], Mária IMECS[3]

[1] Department of Electrical Machines and Drives, Faculty of Electrical Engineering, Technical University of Cluj-Napoca,
e-mail: janos_ferencz@yahoo.com
[2] Department of Electrical Engineering, Faculty of Technical and Human Sciences, Sapientia-Hungarian University of Transylvania, Târgu Mureș,
e-mail: kandras@ms.sapientia.ro
https://orcid.org/0000-0002-6433-2712
[3] Department of Electrical Machines and Drives, Faculty of Electrical Engineering, Technical University of Cluj-Napoca, e-mail: maria.imecs@emd.utcluj.ro

Manuscript received October 15, 2022; revised December 06, 2022

Abstract: The paper presents a strategy of energy loss minimization within a hybrid energy storage system of an electrical vehicle, composed by a battery and a supercapacitor. The optimization of the power sharing between these energy storage devices is performed for the New European Driving Cycle, using the Particle Swarm Optimization algorithm. The minimum energy storage required to pass through the driving cycle is taken into account as a time-variable constraint during the optimization. The dimension of the search space increases with the dimension of the optimization vector, which has to be kept low in order to keep the complexity of the problem manageable. It is shown, that the subdivision, and piecewise optimization of the driving cycle improves the result by means of relaxation of the constraint represented by minimum level of the required energy storage.

Keywords: Particle swarm optimization, hybrid energy storage system, electric vehicle, constrained optimization, New European Driving Cycle.

1. Introduction

In order to take advantage of the high energy storage capability of the batteries and high power capability of the supercapacitors, in electric vehicles these energy storage devices are combined into Hybrid Energy Storage Systems (HESS) [4] [7], [14]. An energy management algorithm has to be implemented to determine the optimal power sharing between the battery and the supercapacitor in order to minimize the energy losses and to extend the battery life cycle [9], [12], [13].

Due to the complexity of the optimization problem, the stochastic Particle Swarm Optimization (PSO) method is a good candidate for solving this task. There is a vast literature on PSO applying different methods for handling the constraints [2], [3], [5], [6], [10], [11].

In [16], [17] we introduced a constrained particle swarm optimization (PSO) algorithm [15], [18], [19] to minimize the energy losses of a HESS from an electric vehicle, for a simple driving cycle. In this paper an extension of the PSO is presented for the standard New European Driving Cycle (NEDC) [20].

2. The Optimization Problem

The model considered for the simulation and optimization of the electrical energy management is shown in *Fig. 1*. The hybrid energy storage system consists of a battery, a supercapacitor and the bidirectional power electronic converters connecting them to the same DC busbar, and providing the possibility of power sharing between the storage devices. Energy exchange between the battery and the supercapacitor has not been considered in this study.

The instantaneous electrical power requirement is derived from the instantaneous acceleration and speed along the driving cycle, the vehicle parameters, and the electrical efficiency of the HESS. In this study, the converter and electric drive losses have been omitted in order to emphasize the effect of the losses in the storage devices.

In the model, the battery voltage u_{BAT} is constant, while the internal resistance r_{BAT} depends on its state of charge *SOC* [1], [8], [11]. The internal resistance r_{SC} of the supercapacitor is constant, while its voltage u_{SC} varies with its state of energy *SOE*. The HESS parameters are shown in *Table 1*.

The vehicle model parameters used for simulation, specified in *Table 2*, correspond to a Tesla Model 3. However, the electrical energy storage devices and their initial charge have been chosen to limit the vehicle range close to the driving cycle length. Thus, the capacity of the battery is 120% of the energy needed to pass through the NEDC driving cycle, and its initial SOC is 83.3%. The energy storage capacity of the supercapacitor is 20% of that of the battery, and it’s initial SOE is 50%.

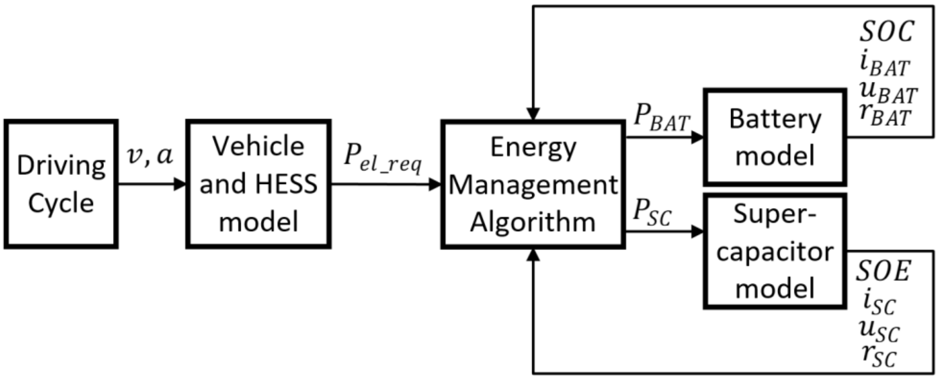

Figure 1: The block diagram of the model considered for the optimal control of the hybrid energy storage system [16].

Table 1: The parameters of the HESS, used for simulation.

Battery	Capacity	Q_{wh}	1.31 kWh
	No load voltage	u_{BAT}	800 V
	Initial state of charge	SOC_{init}	83.3 %
	Internal resistance at SOC=100%	$r_{BAT}\|_{SOC=100\%}$	600 mΩ
	Internal resistance at SOC=50%	$r_{BAT}\|_{SOC=50\%}$	1,05 mΩ
Supercapacitor	Capacity	C_{SC}	2.95 F
	Initial voltage	U_{SC_init}	566 V
	Internal resistance	r_{SC}	100 mΩ

Table 2: The parameters of the vehicle, used for simulation.

Mass of the vehicle	m	1611 kg
Air density	ρ_{air}	$1.202\ \frac{\mathrm{kg}}{\mathrm{m}^3}$
Aerodynamic drag coefficient	C_d	0.3
Maximum cross-section area	$A_{vehicle}$	2.22 m^2
Rolling resistance coefficient	$f_{vehicle}$	0.011

The optimization problem being studied is the optimal power sharing between the energy storage devices for minimum power losses in the HESS over a partition of the driving cycle. In the following, either a single partition (the entire driving cycle) or multiple partitions are being used, with subdivision of each partition into two segments. The optimization vector in each partition is formed by the power shares of the supercapacitor in the two subintervals, defined by (1), extended with the length of the first subinterval normalized to the length of the partition [16].

$$x(t) = \frac{p_{SC\_req}(t)}{p_{el\_req}(t)}. \tag{1}$$

Thus, the optimization task is to find is to find the extended optimization vector

$$\boldsymbol{x}_m^* = [x_1, x_2, \tau]_m = \arg\min_{\boldsymbol{x}^*}(W_{loss}), x_{1,2} \in [0,1], \tau \in [0,1] \tag{2}$$

In this way the dimension of the solution space is only 3, and the complexity of the problem is moderate [16].

In the following, this approach is applied to the whole driving cycle ("global optimization") and subsequently to each partition of the driving cycle ("piecewise optimization") to improve the result of the global optimization.

3. Global Optimization

The stochastic Particle Swarm Optimization (PSO) method is applied for the energy loss minimization in order to handle the problem complexity arising from the nonlinearity of the electric vehicle model including the HESS, the length of the driving cycle, and the multitude of local minima of the cost function W_{loss}.

The minimum energy storage required to pass through the driving cycle is taken into account as a time-variable constraint during the optimization.

Fig. 2 shows the vehicle velocity and acceleration along the New European Driving Cycle (NEDC). Based on the vehicle model, and on the estimated worst-case minimum of the hybrid energy storage system efficiency, the required mechanical and electrical power is calculated. The energy storage needed to pass through the driving cycle is derived as well. Further on, this storage requirement is reduced due to the optimization results, allowing for the relaxation of the minimum stored energy constraint.

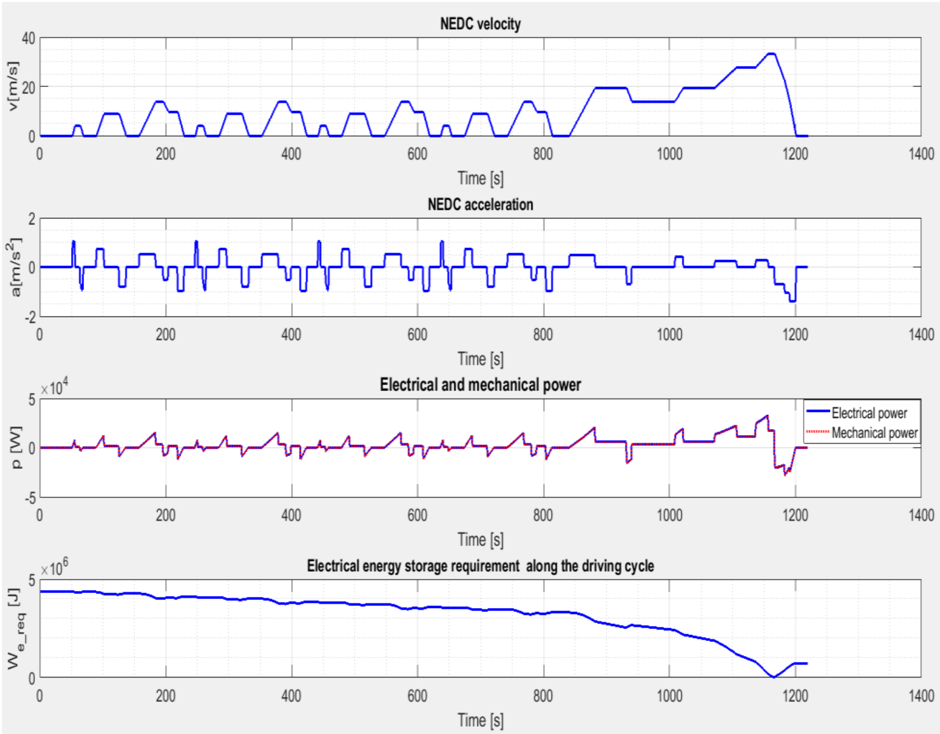

Figure 2: The NEDC velocity and acceleration (top); the power and electrical energy requirement along the driving cycle (bottom).

The flowchart of the global optimization algorithm is shown in *Fig. 3*. The energy storage is initialized according to the initial estimation of the electrical efficiency over the whole driving cycle. The particle swarm optimization is performed over the entire driving cycle using the optimization variable $[x_1, x_2, \tau]$ as shown in *Fig. 4*. Thus, the entire NEDC is subdivided into two time-intervals with constant power sharing ratio. Both the power sharing ratios and the time instant of the subdivision are elements of the optimization variable. The corresponding particle swarm optimization (PSO) algorithm is described in detail in [16]. The number of individuals in the swarm is 25, and a number of 8 constraints are applied during the optimization, including the minimum required energy storage, as a time function. The result of the optimization cycle is a better electrical efficiency, than initially assumed, thus the constraint regarding the required energy storage can be modified, extending the available search space, and thus improving the result of the next optimization cycle. A few such optimization cycles are performed until the efficiency increment using this method becomes negligible.

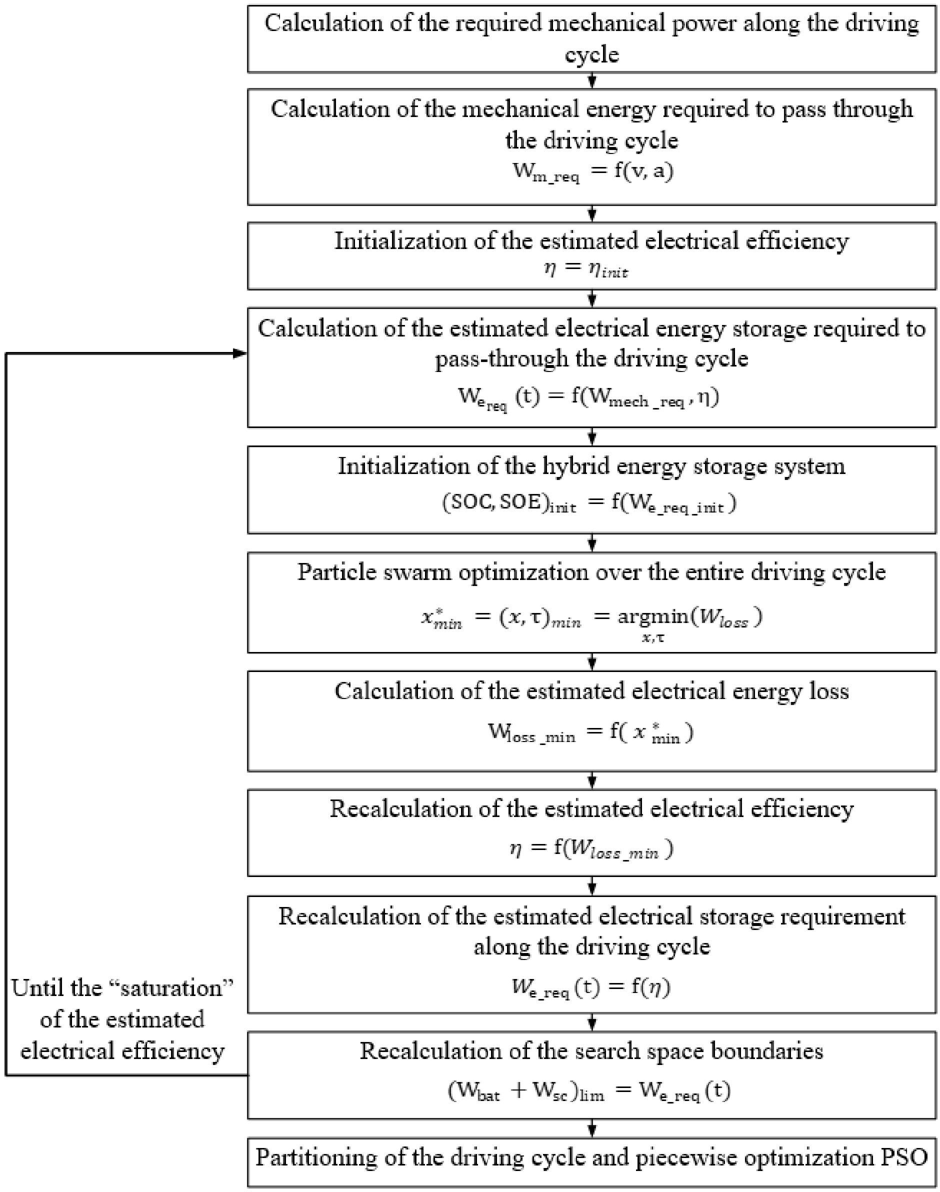

Figure 3: Flowchart of the global efficiency optimization algorithm.

Fig. 5 explains the evolution with the number of successive iterations of the required energy storage versus time, while *Fig. 6* illustrates the evolution of the estimated efficiency with the number of optimization cycles.

Further reduction of the HESS losses can be obtained by piecewise optimization over the partition of the driving cycle, as explained in the next section.

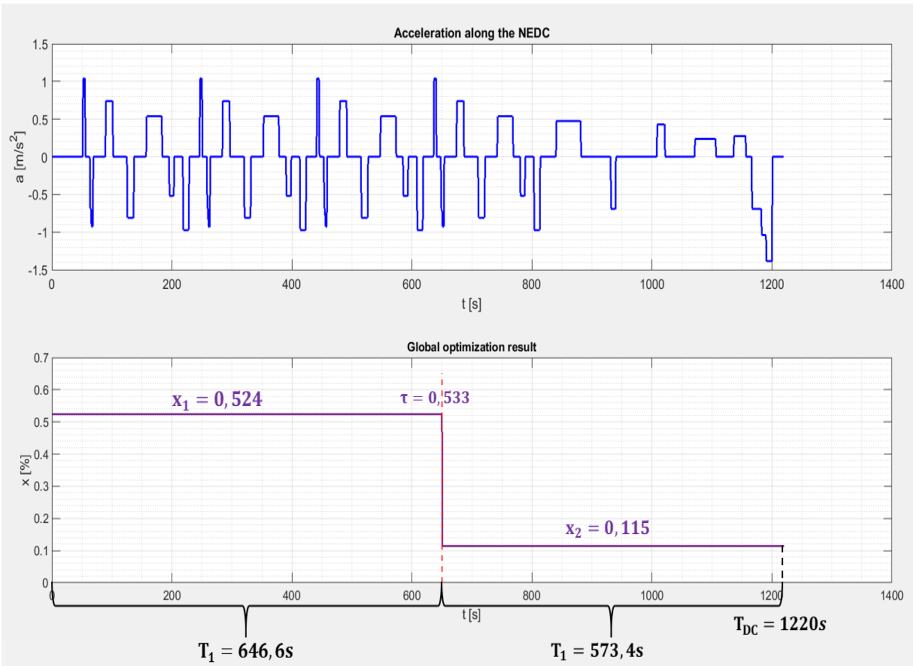

Figure 4: The NEDC acceleration profile (top), and the interpretation of the global optimization vector (bottom): $x^*_{\min} = (x_1, x_2, \tau) = (0.524, 0.115, 0.533)$.

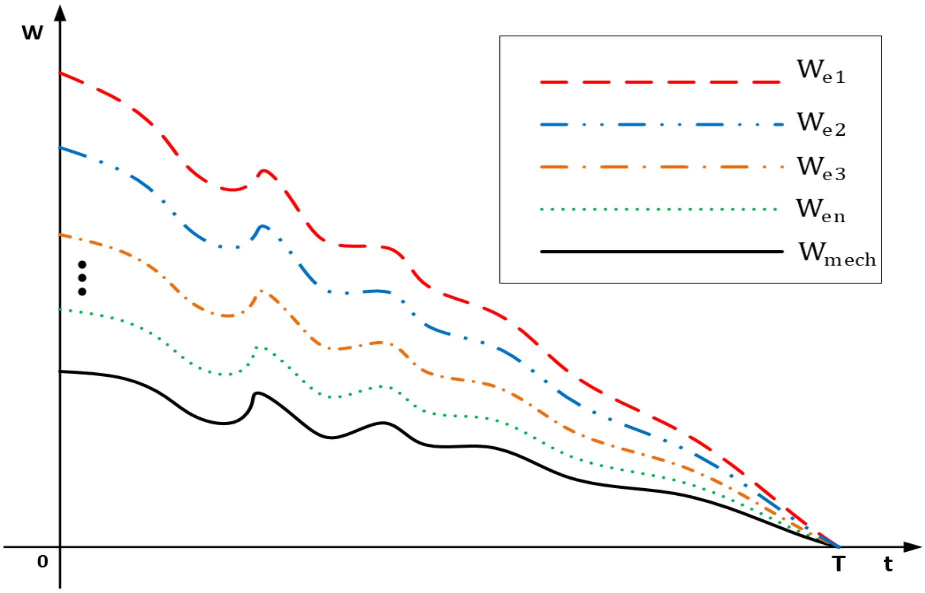

Figure 5: Variation of the energy storage requirement along the driving cycle with the number of iterations of the global efficiency optimization algorithm.

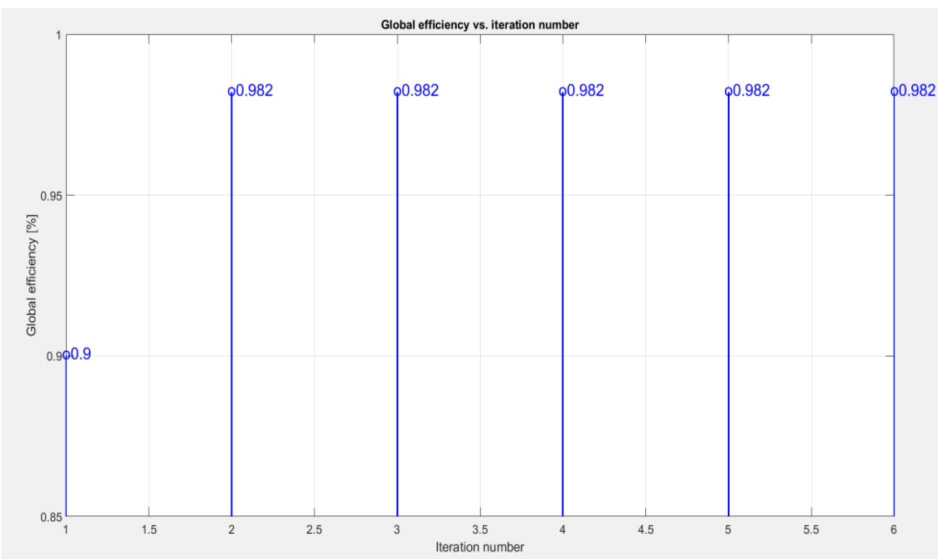

Figure 6: Variation of the global efficiency of the HESS vs. the number of global optimization iterations.

4. Piecewise Optimization

The dimension of the search space increases with the dimension of the optimization vector, which has to be kept low in order to keep the complexity of the problem manageable. It is shown, that the subdivision, and piecewise optimization of the driving cycle improves the result by means of relaxation of the constraint represented by the minimum level of the required energy storage.

The partitioning of the driving cycle can be made in multiple ways, and the advantages of each still have to be analyzed. During this study it has been observed that a partitioning at positive zero-crossing instants of the acceleration curve yields better results, than other trials (ex. at negative zero-crossings of the acceleration, at positive or negative zero-crossings of the required instantaneous power, or equidistant partitioning), consequently this is the approach used for the piecewise optimization, as shown in *Fig. 7*.

Each route section resulting from the partition is subdivided into two time-intervals, and the PSO algorithm is applied using the optimization vector formed by the power sharing ratios and the relative position of the subdivision. In the k-th partition, the optimization vector is $\boldsymbol{x} = (x_{1k}, x_{2k}, \tau_k)$, where $\tau_k = \frac{\boldsymbol{T_{1k}}}{\boldsymbol{T_{1k}+T_{2k}}}$, as shown in *Fig. 7*.

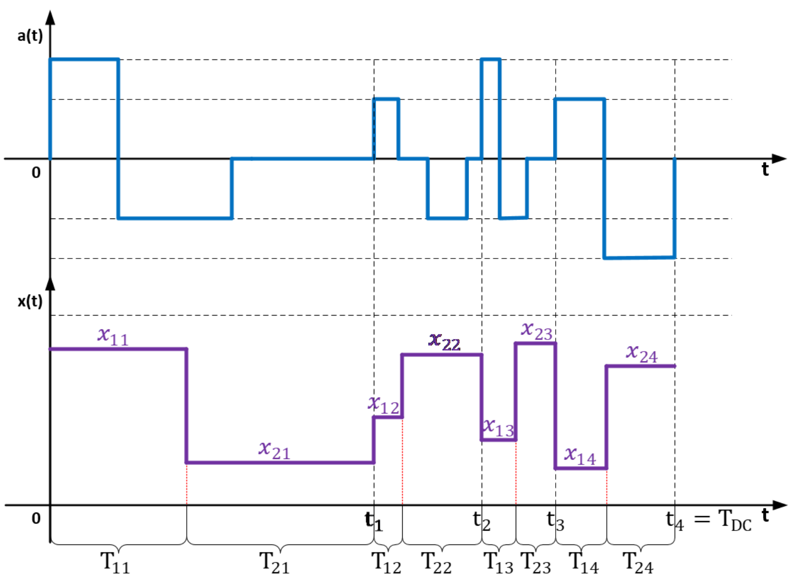

Figure 7: Illustration of the driving cycle partitioning and the optimization vector components along different route sections.

The flowchart of the piecewise optimization algorithm is shown in *Fig. 8*.
The energy saving ΔW_{es_k} obtained along the k-th route section is subtracted from the required energy storage in the $(k+1)$-th route section, thereby extending the available search space. This principle is illustrated in *Fig. 9*, where $W_e(t)$ is the energy consumption estimated using the efficiency obtained by global optimization, while $W_e^*(t)$ is the energy consumption obtained by piecewise optimization, updating the energy storage requirement after each route section.

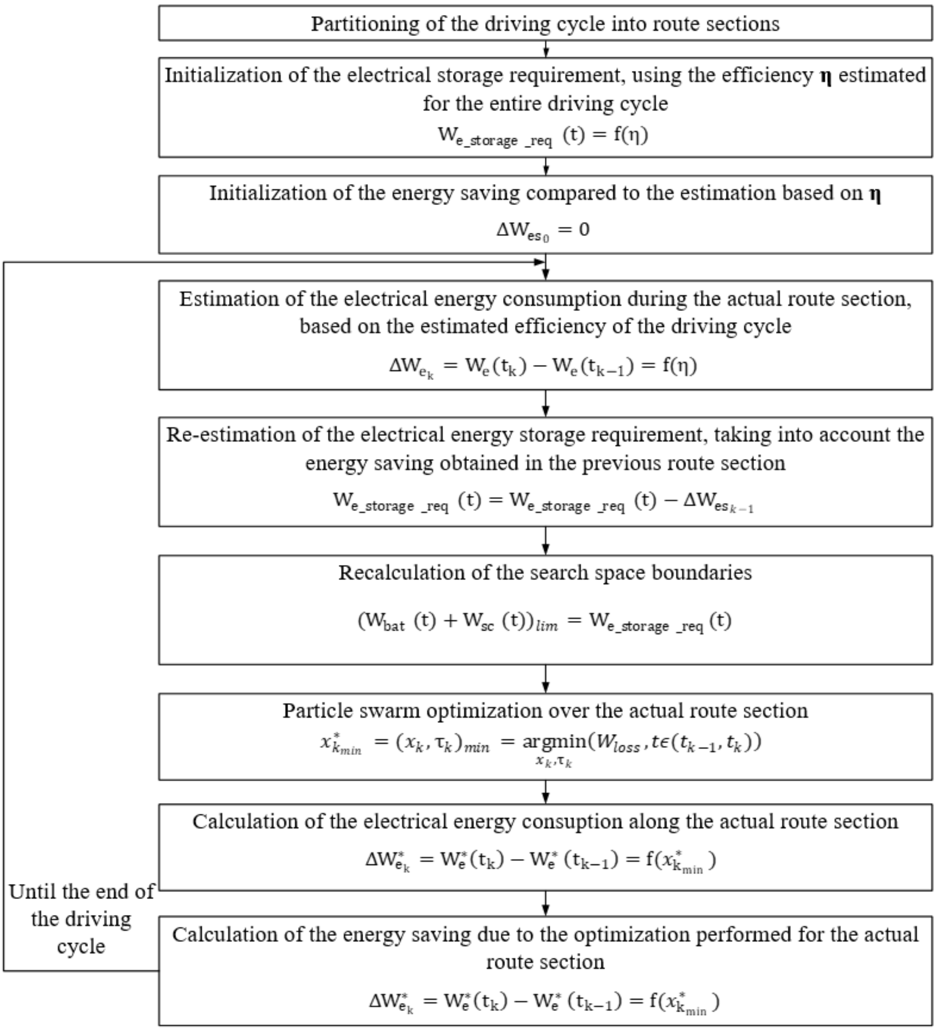

Figure 8: Flowchart of the piecewise optimization algorithm, which extends the search space of each route section due to the "energy saving" from the previous section.

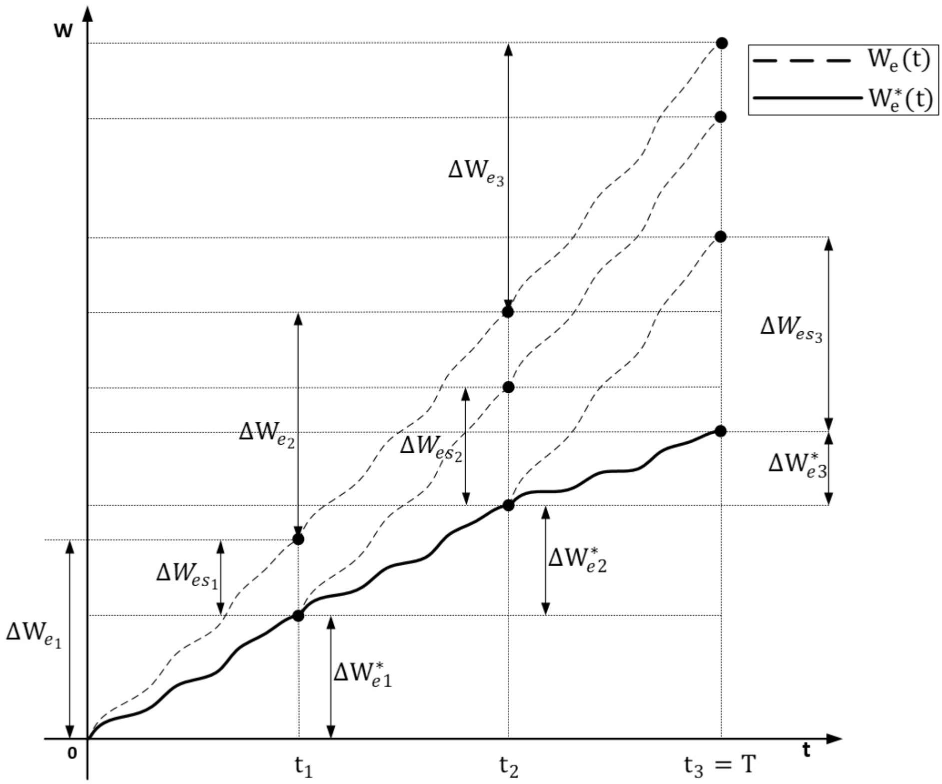

Figure 9: Time diagram for the illustration of the piecewise optimization algorithm. The continuous line represents the effective energy consumption, while the dashed lines represent energy consumptions assuming no piecewise optimization in the final sections of the route.

Fig. 10 illustrates the evolution of the piecewise optimization vector components along the driving cycle, while *Fig.11* shows the energy saving in each route section.

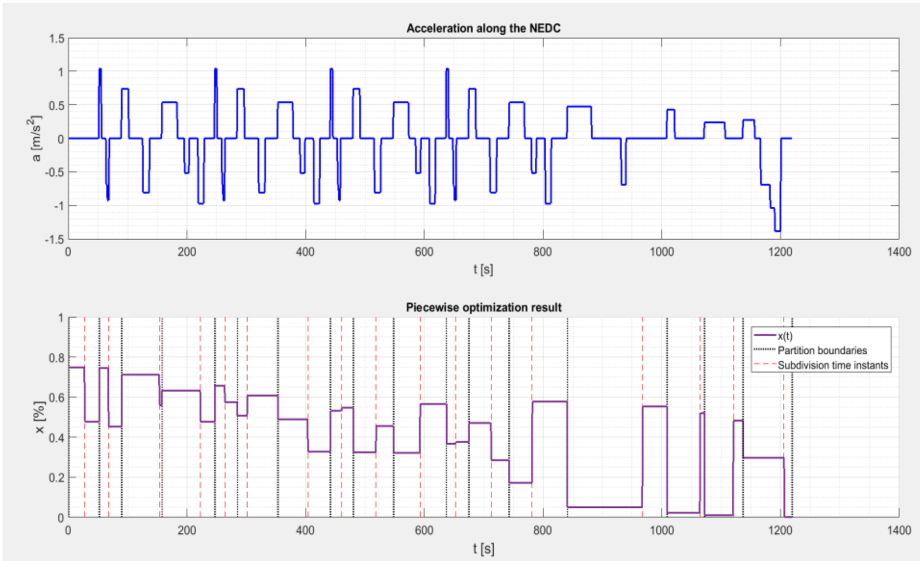

Figure 10: The NEDC acceleration profile (top), and the components of the piecewise optimization vector (bottom).

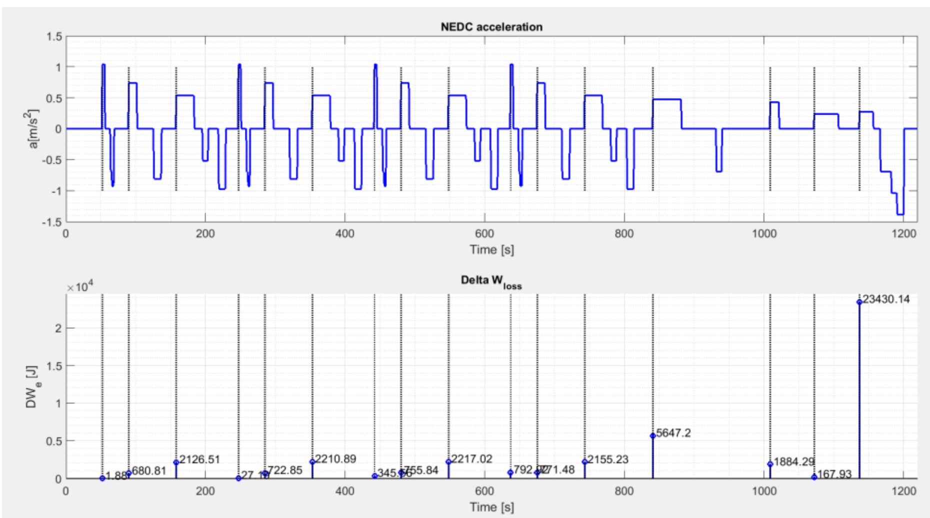

Figure 11: The NEDC acceleration profile (top) and the "electrical energy saving" along each route section (bottom).

The evolution of the battery state of charge (SOC) and of the supercapacitor state of energy (SOE) along the driving cycle is presented in *Fig. 12* for both the global and the piecewise optimization cases.

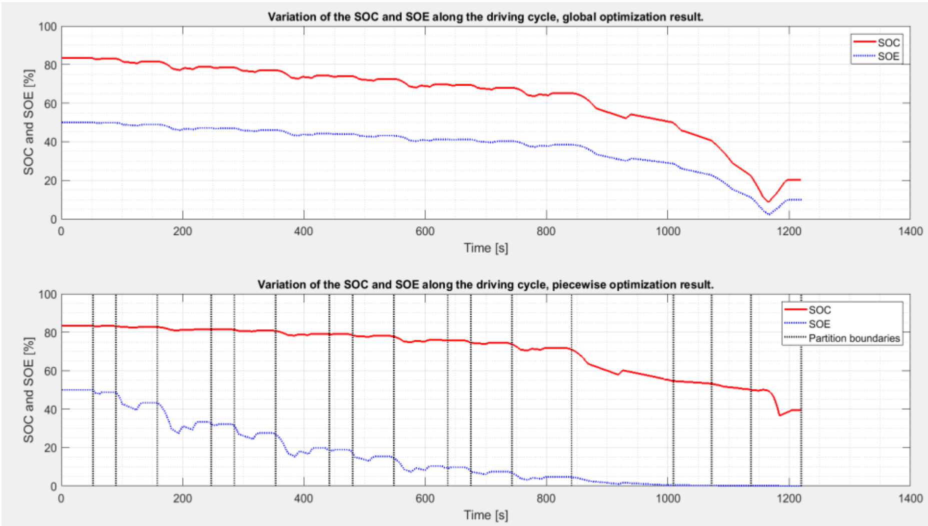

Figure 12: Variation along the driving cycle of the battery state of charge (SOC) and supercapacitor state of energy (SOE) in the global optimization (top) and piecewise optimization (bottom) cases.

Fig. 13 provides a proof of the improvement brought by the application of the piecewise optimization on top of the global optimization result.

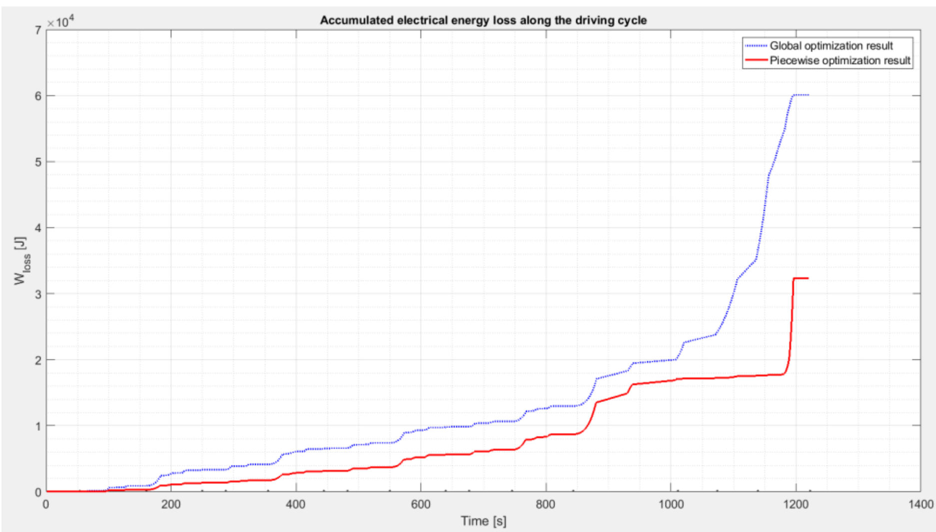

Figure 13: The accumulated electrical energy losses in the HESS along the driving cycle, in the global and piecewise optimization cases.

5. Conclusions

In the paper it has been shown that the energy loss minimization of a hybrid energy storage system over a standard driving cycle of an electric vehicle can be successful applying a low-dimensional optimization vector. The optimization has been performed in two steps: an iterative global optimization and a piecewise optimization of the partitioned route. In both cases the result of the stochastic search is improved step-by-step due to the knowledge gain about the energy requirement in previous optimization steps. Thus, a feed-back about the entire route yields the relaxation of the constraints and allows for better search results.

The detailed analysis of the driving cycle partitioning strategy remains a subject for future work.

References

[1] Chen, Q., Jiang, J., Ruan, H., and Zhang, C., “Simply Designed and Universal Sliding Mode Observer for The SOC Estimation of Lithium-Ion Batteries”, IET Power Electronics, vol. 10 Iss. 6, pp. 697−705, Jan. 2017.

[2] Huang, T., and Mohan, A. S., “A Hybrid Boundary Condition for Robust Particle Swarm Optimization”, *IEEE Antennas and Wireless Propagation Letters*, vol. 4, pp. 112−117, Jun. 2005.

[3] Wang, D., Tan D., and Liu, L., “Particle Swarm Optimization Algorithm: An Overview”, *Springer Link. Soft Computing*, vol. 22, pp. 387−408, Jan. 2017.

[4] Kanglong, Y., Peiqing, L., and Hao, L., “Optimization of Hybrid Energy Storage System Control Strategy for Pure Electric Vehicle Based on Typical Driving Cycle”, *Hindawi. Mathematical Problems in Engineering*, vol. 2020, pp. 1−12, Jun. 2020.

[5] Chong, L., W., Wong, Y., W., and Rajkumar, R., K., “An Optimal Control Strategy for Standalone PV System with Battery Supercapacitor Hybrid Energy Storage System”, *Elsevier. Journal of Power Sources*, vol. 331, pp. 553−565, Nov. 2016.

[6] Ammari, C., Belatrache, D., Touhami, B., and Makhlouf, S., “Sizing, Optimization, Control and Energy Management of Hybrid Renewable Energy System — A Review”, *KeAi. Energy and Built Environment*, vol. 2, pp. 23−-53, Aug. 2021.

[7] Romaus, C., Gathmann, K., and Böcker, J., “Optimal energy management for a hybrid energy storage system for electric vehicles based on stochastic dynamic programming”, *2010 IEEE. Vehicle Power and Propulsion Conference*, pp. 1−6, Sept. 2010.

[8] Vinot, E., and Trigui, R., “Optimal Energy Management of HEVs with Hybrid Storage System”, *HAL open science. Energy Conversion and Management*, vol. 76, pp. 437−452, Feb. 2019.

[9] Capassoa, C., Lauria, D., and Veneria, O., “Optimal Control Strategy of Ultra-Capacitors in Hybrid Energy Storage System for Electric Vehicles”, *Elsevier. Energy Procedia*, vol. *142*, pp. 1914–1919, Aug. 2017.

[10] Sadeq, T., Wai, C., K., Morris, E., Tarbosh, Q., A., and Aydoğdu, Ö., “Optimal Control Strategy to Maximize the Performance of Hybrid Energy Storage System for Electric Vehicle Considering Topography Information”, *IEEE Access*, vol. 8, pp. 1−13, Nov. 2020.

[11] Chang, W. Y., “The State of Charge Estimating Methods for Battery: A Review”, *Hindawi. International Scholarly Research Notices*, vol. 2013, pp. 1–8, Jul. 2013.

[12] Ye, K., and Li, P., "A New Adaptive PSO-PID Control Strategy of Hybrid Energy Storage System for Electric Vehicles", *Sage. Advances in Mechanical Engineering*, vol. 12, pp. 1-15, Aug. 2020.

[13] Ferencz, J., Kelemen, A., and Imecs, M., "Control of an Electric Vehicle Hybrid Energy Storage System", *Sciendo, Papers on Technical Science*, vol. 14, pp. 77-88, Aug. 2021.

[14] Paul, T., Mesbahi, T., and Durand, S., "Sizing of Lithium-Ion Battery/Supercapacitor Hybrid Energy Storage System for Forklift Vehicle", *Energies*, vol. 13, pp. 1-18, Sep. 2020.

[15] Borgulya, I., "Optimalizálás Evolúciós Számításokkal", Typotex Kiadó Budapest, 2011.

[16] Ferencz, J., and Kelemen, A., „Particle Swarm Optimization of a Hybrid Energy Storage System", *Acta Universitatis Sapientiae, Electrical and Mechanical Engineering*, vol. 13, pp. 82-100, Dec. 2021.

[17] Ferencz, J., Kelemen, A., and Imecs, M., "Particle Swarm Optimization of an Electric Vehicle Hybrid Energy Storage System", *ANNALS of Faculty Engineering Hunedoara, International Journal of Engineering*, vol. 20, pp. 23-30, Aug. 2022.

[18] Das, S., Abraham, A., and Konar, A., "Particle Swarm Optimization and Differential Evolution Algorithms: Technical Analysis, Applications and Hybridization Perspectives", *International Journal of Computational Intelligence Studies*, vol. 116, pp. 1-38, May. 2008.

[19] Tharwat, A., Gaber, T., Hassanien, AE., and Elnaghi, BE., "Handbook of Research on Machine Learning Innovations and Trends", publisher: IGI Global, pp. 614-635, 2017.

[20] Barlow, TJ., Latham, S., McCrae, IS., and Boulter, PG, "A reference book of driving cycles for use in the measurement of road vehicle emissions", publisher: IHS, pp. 7-13, Jun. 2009.

Acta Universitatis Sapientiae

The scientific journal of Sapientia Hungarian University of Transylvania (Cluj-Napoca, Romania) publishes original papers and surveys in several areas of sciences written in English.
Information about each series can be found at
`http://www.acta.sapientia.ro`.

Acta Universitatis Sapientiae
Electrical and Mechanical Engineering

Sapientia University

Scientia Publishing House

ISSN 2065-5916
http://www.acta.sapientia.ro

Information for authors

Acta Universitatis Sapientiae, Electrical and Mechanical Engineering publishes only original papers and surveys in various fields of Electrical and Mechanical Engineering. All papers are peer-reviewed.

Papers published in current and previous volumes can be found in Portable Document Format (PDF) form at the address: `http://www.acta.sapientia.ro`.

The submitted papers must not be considered to be published by other journals. The corresponding author is responsible to obtain the permission for publication of co-authors and of the authorities of institutes, if needed. The Editorial Board is disclaiming any responsibility.

The paper must be submitted both in MSWord document and PDF format. The submitted PDF document is used as reference. The camera-ready journal is prepared in PDF format by the editors. In order to reduce subsequent changes of aspect to minimum, an accurate formatting is required. The paper should be prepared on A4 paper (210×297 mm) and it must contain an abstract of 200-250 words.

The language of the journal is English. The paper must be prepared in single-column format, not exceeding 12 pages including figures, tables and references.

For submission and the template file visit the following address:
`http://www.acta.sapientia.ro/acta-emeng/emeng-main.htm`.

One issue is offered to each author free of charge. No reprints are available.

Contact address and subscription:
Acta Universitatis Sapientiae, Electrical and Mechanical Engineering
Sapientiae Hungarian University of Transylvania
RO 400112 Cluj-Napoca
Str. Matei Corvin nr. 4.
E-mail: acta-emeng@acta.sapientia.ro

Printed by F&F INTERNATIONAL
Director: Enikő Ambrus

Supported by:

Megvalósult a Magyar Kormány Támogatásával
Miniszterelnökség Nemzetpolitikai Államtitkárság
Bethlen Gábor Alap